IDENTIFYING AREAS OF NEOTECTONIC ACTIVITY USING RADAR REMOTE SENSING IN THE NORTHERN FOOTHILLS OF THE ALASKA RANGE

By

Casey L. Denny

RECOMMENDED:

Advisory Committee Chair

Chair, Department of Geology and Geophysics

APPROVED:

Dean, College of Natural Science and Mathematics

Dean of the Graduate School

29 April 2013

Date

IDENTIFYING AREAS OF NEOTECTONIC ACTIVITY USING RADAR REMOTE SENSING IN THE NORTHERN FOOTHILLS OF THE ALASKA RANGE

A

THESIS

Presented to the Faculty

of the University of Alaska Fairbanks

in Partial Fulfillment of the Requirements

for the Degree of

MASTER OF SCIENCE

By

Casey L. Denny, B.T.

Fairbanks, Alaska

May 2013

ABSTRACT

The tectonically active northern foothills of the Alaska Range display obvious uplift and deformation, making the area an attractive place to conduct research. Research has been done in this area of Alaska in the recent past, most of which required intensive fieldwork. This study analyzes if modern radar remote sensing technology is useful in identifying neotectonic activity and in determining where future work should be conducted. Radar remote sensing data is used in two ways to support the identification of tectonically active areas: First, I incorporated available geologic maps with polarimetric and interferometric radar remote sensing data to create a classification scheme to identify and map the preserved depositional surface of the Nenana Gravel. This surface, successfully mapped and overlain on a newly available high-resolution DEM, highlighted the topographic expression of deformation in the area. Second, the high-resolution DEMs were used to create and analyze longitudinal river profiles, and a Stream Length-Gradient Index Map, both of which correlate well with known active structures. This study indicates that radar remote sensing can be used to identify tectonically active areas before employing extensive fieldwork and used in combination with traditional geological procedures enhances the amount and quality of the derived information.

TABLE OF CONTENTS

Page

LIST OF FIGURES

Page

LIST OF TABLES

Page

LIST OF ACRONYMS

ALOS – Advanced Land Observing Satellite

ANOVA - Analysis of Variance

ASF – Alaska Satellite Facility

AVNIR-2 - Advanced Visible and Near Infrared Radiometer type 2

DEM – Digital Elevation Model

DOGS-AP - DSM and Ortho-rectified image Generation Software for ALOS PRISM

DSM – Digital Surface Model

DTM – Digital Terrain Model

EM – Electromagnetic

ERS – European Remote-sensing Satellite

ESA – European Space Agency

ETM+ – Enhanced Thematic Mapper

GINA – Geographic Information Network of Alaska

GPS – Global Positioning System

HH – Horizontal (transmit) Horizontal (receive polarization)

HV – Horizontal (transmit) Vertical (receive polarization)

InSAR – Interferometric SAR

Isodata - Iterative Self-Organizing Data Analysis Techniques A^2

JAXA – Japan Aerospace Exploration Agency

NaN – Not a Number

NASA - National Aeronautics and Space Administration

NED – National Elevation Dataset

NLCD - National Land Cover Database

PALSAR – Phased Array L-band Synthetic Aperture Radar

PolSAR –Polarimetric SAR

PRISM – Panchromatic Remote-sensing Instrument for Stereo Mapping

RTC – Radiometric Terrain Correction

SAR – Synthetic Aperture Radar

SDMI – Statewide Digital Mapping Initiative

SRTM – Shuttle Radar Topography Mission

TM – Thematic Mapper

USGS – United States Geologic Survey

VH – Vertical (transmit) Horizontal (receive polarization)

VV – Vertical (transmit) Vertical (receive polarization)

ACKNOWLEDGEMENTS

The completion of this work could not have been possible without the generous support of the Alaska Satellite Facility, and its team of people that created and supported the MapReady program. I would like to thank my advisors Franz Meyer, Wes Wallace and Rudi Gens, for their help and support during the duration of the project. Finally nothing would have been possible without the continual support from my family, officemates and friends.

1.0 Introduction

The tectonically active northern foothills of the Alaska Range display obvious uplift and deformation of geomorphic surfaces, making the area an attractive place to conduct research. However the foothills are remote and difficult to access, causing fieldwork to not only be challenging but expensive, making the area an ideal place to use remote sensing techniques. Remote sensing techniques have been used for many years to delineate neotectonic features in developing fold and thrust belts throughout the world. The areas where remotely sensed data is highly effective, however, are typically arid climates and/or barren terrains, where the effects of vegetation and moisture are limited. Remote sensing-based methods also rely heavily on high quality surface topography information to retrieve reliable information. Consistent high quality elevation data is often confined to the area of the Earth between 56 degrees south and 60 degrees north. This area was covered by the Shuttle Radar Topography Mission (SRTM), which resulted in a 30-meter resolution elevation map covering 80 percent of the Earth's surface (Farr et al., 2007). For areas north or south of the SRTM coverage, high-resolution elevation data is commonly scarce or outdated. In many areas of rural Alaska, the best available elevation data is derived by interpolation from topographic maps to a resolution of 60 meters (Gesch et al., 2009), effectively limiting remote analysis of subtle neotectonic features within the higher latitudes. These limitations can be mitigated by using new remote sensing products such as recently released Interferometric SAR (InSAR) derived Digital Elevation Models (DEM) as well as

Polarimetric SAR (PolSAR) data. I will show that both InSAR and PolSAR data are useful in identifying and mapping tectonically active surfaces in my area of interest. PolSAR data is used in this study to identify Preserved Nenana Gravel surface, which is a depositional surface that has been uplifted and deformed in the northern foothills throughout the recent geologic past. InSAR data is used to create high resolution digital elevation models (DEMs). These DEMs are used to calculate known geomorphic indices for the area of interest. The high quality of these new DEMs allowed me to pinpoint areas of active deformation, which may have been overlooked by the use of coarser DEMs and the limited satellite data available in the area.

Previous work in the northern foothills area has concluded that this area is an active fold-and-thrust belt (Bemis and Wallace, 2007; Lesh and Ridgway, 2007; Bemis et al., 2012). This conclusion was reached by analyses completed on antiquated Digital Elevation Models that were based on survey maps completed in the 1950's and surface geologic maps derived from limited ground observation and aerial photo interpretation (Wahrhaftig, 1953; Wahrhaftig, 1970a-h; Bemis and Wallace, 2007; Lesh and Ridgway, 2007). The elevation data is relatively accurate in the horizontal direction. However, the same elevation data is less accurate in the vertical range, and the surface geologic maps are based on aerial photographs that can be difficult to interpret due to clouds and vegetation. Other studies completed in the area included fieldwork, which while necessary, is expensive in this remote portion of Alaska. I will show that by utilizing

modern remotely sensed data the amount of fieldwork can be constrained to studying areas of interest instead of finding the areas that would be considered interesting.

1.1 Objectives

The objective of this study is to utilize new remote sensing data processing techniques to identify areas of neotectonic activity in the northern foothills of the Alaska Range. It is designed to demonstrate the capability of these techniques to identify regions of high activity within a large area so future research efforts and fieldwork can be focused where it counts. This objective is achieved by using (1) polarimetric SAR data to map the extent of the preserved upper depositional surface of the Nenana Gravel. The Nenana Gravel forms an extensive geomorphic surface that has been uplifted and deformed by faults and folds related to the tectonic growth of the Alaska Range and propagation of the associated fold and thrust belt into the foreland basin. To identify Nenana Gravel surfaces from the data, a multi-step processing procedure was developed that combines radiometric and polarimetric pre-processing steps with a supervised image classification method. This study also assesses how well classification rules developed using local training sites can be transferred to the rest of the study area. If successful, the data that represents the preserved surface of the Nenana Gravel can be extracted for further geologic analysis. (2) Newly available high resolution DEM's will be used to extract longitudinal river profiles, which will then be visually analyzed for evidence of tectonic

activity. Finally (3) a Stream Length-Gradient Index will be calculated from the derived longitudinal river profiles and the resulting values will be interpolated over the region and incorporated with current fault and fold data to determine local areas of activity.

1.2 Hypotheses

This study uses state of the art satellite technologies in the microwave range and will base the elevation data on real earth measurements, not interpolation from survey maps. It is hypothesized that (1) using new technologies will improve the data found by previous researchers who did extensive fieldwork but were dependent on coarse or antiquated remote sensing information and (2) information extracted from polarimetric and interferometric radar remote sensing data can be used to identify areas of neotectonic deformation in the northern Foothills of the Alaska Range.

2.0 Location and Geologic Background

2.1 Location

The Alaska Range extends over 1,000 kilometers from the Alaska Peninsula in the west to the Canadian border to the east in a northward-convex arc. The range is dominated by large features such as the Denali fault and a profusion of large mountains such as Mount McKinley (Denali), which stands at 6,194 meters and is the tallest peak in North America. Just to the north of Denali are lowlands that range in elevation from 150 to 250 meters in elevation, while the Alaska Range displays relatively low topography eastward to the Hayes range, which includes numerous mountains above 3,300 meters (e.g., Mount Deborah (3761 m), Hess Mountain (3639 m) and Mount Hayes (4216 m)). The study area is located where the northern foothills extend in an arc to the north of the zone of relatively low topography in the Alaska Range. Figure 2.1 shows the location of the study area within Alaska and relative to the Alaska Range. The general shape of the foothills mirrors the arcuate form of the central Alaska Range. Two major transportation corridors transect the mountains on either side of the study area. The corridor to the west of the study area follows the Nenana River through the mountains and is home to the Parks Highway and the Alaska Railroad, connecting Alaska's two largest cities, Anchorage and Fairbanks. The other highway to the east of the study area follows the Delta River through the mountains and is home to the Richardson Highway

and the Trans Alaska Pipeline, which carries crude oil from the North Slope to the harbor in Valdez.

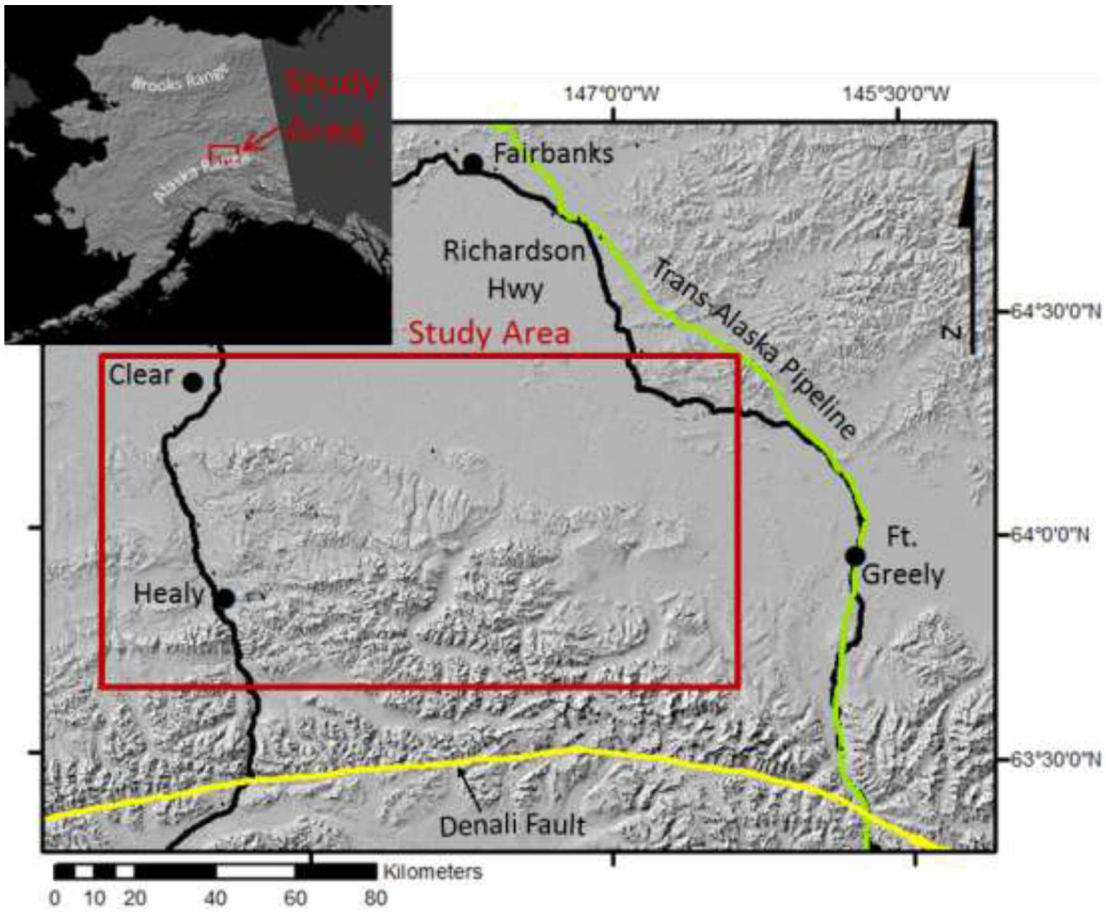

Figure 2.1 Study Area Map. The study area map shows the relation of the study to transportation corridors, military installations, towns and the Denali Fault, which are all located in central Alaska

There are numerous military installations in and around the study area. Clear Air Force Station is a ballistic missile early warning radar site off the Parks Highway, and Fort Greely, located on the Richardson Highway, is an Army launch site for anti-ballistic missiles and an arctic technology test facility.

2.2. Geology

The geology in the area consists of Cenozoic non-marine deposits that overlie the metamorphic basement and have been uplifted and deformed by the growth of the northern foothills fold and thrust belt. Anticlines in the area consist of the deformed Cenozoic sediments cored by basement schist.

2.2.1 Stratigraphic Units

Three main stratigraphic units in the area are important to this study: (1) The Nenana Gravel, which consists of thick alluvial deposits capped by a preserved depositional surface that has been deformed by ongoing neotectonics; (2) The Usibelli Group, that consists of non-marine deposits that unconformably underlie the Nenana Gravel; (3) A variety of schist exposed in the cores of the northern foothills anticlines.

2.2.1.1 Schist Cores

The basement rock of the foothills consists of several different schist units - Healy Schist, Keevy Peak Formation, and the Totatlanika Schist - that are derived from sediments that were deposited from the Early Paleozoic to the Late Devonian – Early Mississippian (Dusel-Bacon et al. 2004; Athey et al., 2006). These schists are structurally thickened and highly deformed and show evidence of multiple episodes of structural thickening and metamorphism (Bemis, 2004).

2.2.1.2 Usibelli Group

The Usibelli Group unconformably overlies the metamorphic rocks and also unconformably underlies the Nenana Gravel (Wahrhaftig, 1953). The unit consists of an assortment of conglomerate, sandstone, mudstone, and coal. Indicators toward the bottom of the unit show that drainage at the time of deposition was to the south, however, higher in the unit they show that the southward flow had shifted toward the west (Lesh and Ridgway, 2007). The coal beds in the unit indicate that this shift resulted in ponding (Triplehorn et al., 2000). The Usibelli Group is interpreted as the depositional system in a foredeep basin that stemmed from early transpressional deformation to the south of the study area that preceded the main shortening and exhumation that resulted in the formation of the present Alaska Range (Ridgway et al., 2007). An ash layer in the upper formation of the Usibelli Group was dated at ~6.4-6.7 Ma (Triplehorn et al., 2000), suggesting that the major portion of the uplift of the Alaska Range started around that time.

2.2.1.3. Nenana Gravel

The Nenana Gravel is the stratigraphic unit of most interest for this study. The Nenana Gravel reaches up to 1200 meters in thickness adjacent to the Alaska Range and thins to the north (Wahrhaftig, 1953; Ridgway et al., 2007). The gravels mainly consist of poorly consolidated, moderately well sorted conglomerate, with pebble sizes of 1-2 inches at

the bottom of the formation and 3-4 inches at the top and a maximum pebble size of 18 inches. The gravels also contain lenses of fine-grained sand. Pebbles are composed of schist, quartzite and sandstone, with some granite and other intrusive rocks. The plutonic rocks in the conglomerates of the lower Nenana Gravel originated from the southern portion of the mountains and the igneous pebbles in the younger Nenana are from the north side of the mountains (Ridgway et al., 2007). This indicates that the foreland basin of the Alaska Range migrated northward during the deposition of the gravels. This northward migration was accompanied by a change in the depositional environment from braided stream to alluvial fan, indicated by the coarsening upwards of the Nenana Gravel in the stratigraphic column (Ridgway et al., 2007). Within the northern foothills, the Nenana Gravel has an exposed and preserved upper depositional surface that was uplifted and deformed. This surface was originally deposited in the foreland basin of the growing Alaska Range and defines the extent of the uplift and deformation associated with the northward-propagating fold and thrust belt. The end of the deposition of these gravels was previously dated as 2.8 Ma (Wahrhaftig, 1987), but this has recently been re-dated to be as young as 1.0 Ma (Athey et al., 2006; Bemis, 2010) and was caused by the propagation of the fold and thrust belt into the region (Bemis and Wallace, 2007).

2.3 Tectonic Setting

The Alaska Range is a north convex arcuate mountain range in central Alaska that parallels the curve of the Denali fault. Although this mountain range is located in central Alaska, it is widely accepted that the subduction of the Pacific plate to the south causes the uplift and northward propagation of the Alaska Range (Bemis and Wallace, 2007; Haeussler, 2008; Bemis et al., 2012). The Pacific plate moves towards the northwest and subducts under Alaska at the Aleutian Trench, at a rate around 5.3 cm/yr (red arrows in figure 2.2) (Freymueller et al., 2008; Haeusseler, 2008). A fraction of this relative motion is accommodated in the Alaska Range by strike-slip movement on the Denali and related faults (blue arrow in figure 2.2). The remaining fraction of relative motion is accommodated by shortening within the fold and thrust belt that trends normal to the range (yellow arrow in figure 2.2). Within the study area, this contraction has formed the northward propagating fold and thrust belt of the northern foothills of the Alaska Range (Hanson et al, 2002; Bemis and Wallace, 2007; Lesh and Ridgway, 2007; Bemis et al., 2012). This northward propagation of the fold and thrust belt indicates a south-dipping basal detachment with a leading edge located in the area of the Northern Foothills thrust. Above this basal detachment a combination of folds and faults accommodates the shortening of the area, with folds that range in size from 600 to 1200 meters in amplitude (Wahrhaftig, 1987). The folds in the area have been modeled, in part, on the remains of the preserved Nenana Gravel surface which was uplifted and

deformed by the thrust belt that moved into the foreland basin (Bemis, 2004; Bemis and Wallace, 2007; Bemis et al., 2012) and could be as young as ~1 Ma.

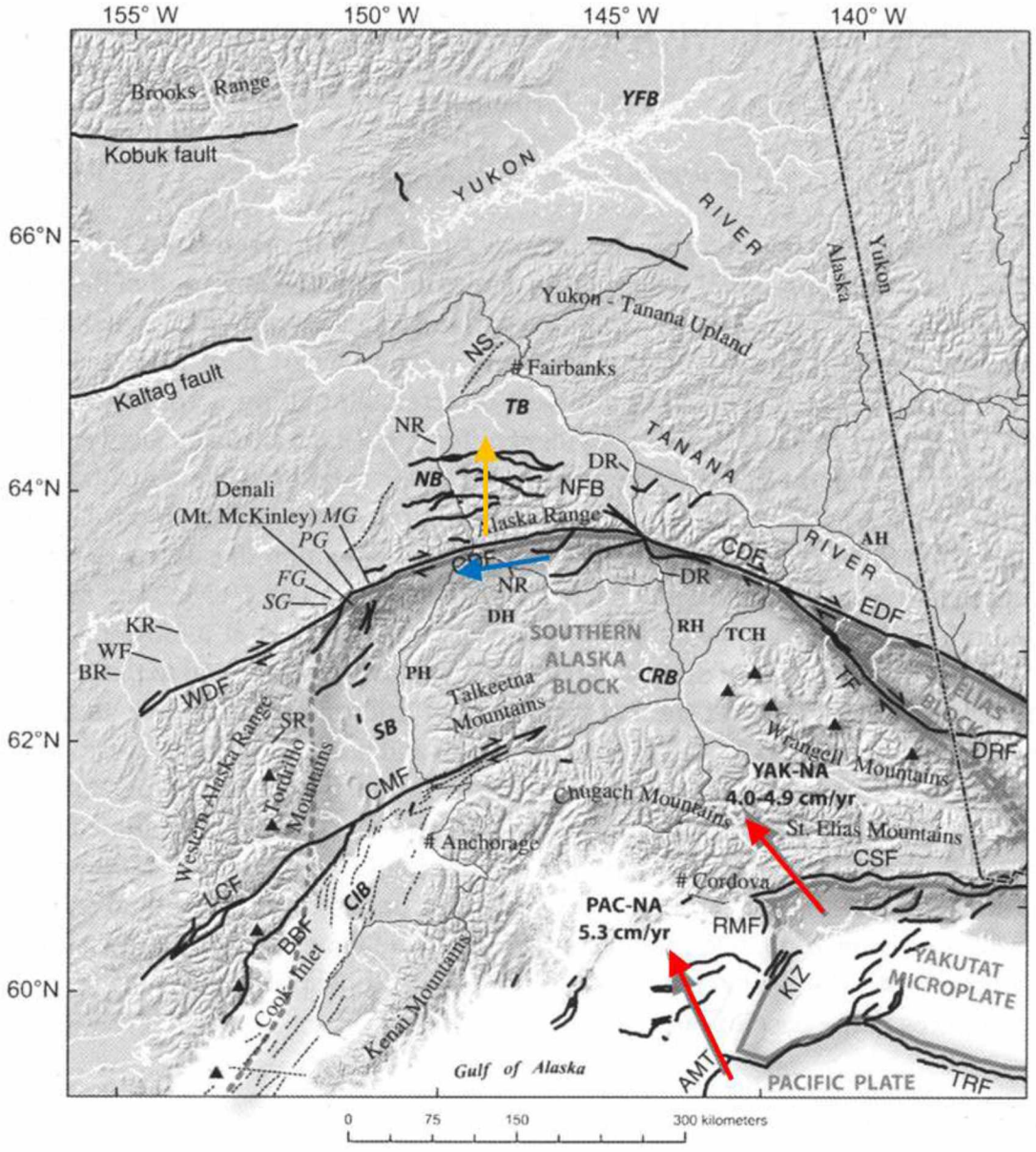

Figure 2.2 Motions Associated with Alaska Range Tectonics. Pacific and Yakutat plate motion, shown in red, is accommodated in two ways within the Alaska Range. The blue or westward motion is accommodated by the Denali fault and the yellow or northward motion by the northern foothills fold and thrust belt. Figure modified from Haeussler, 2008.

The faults associated with the folds are mainly north-vergent thrusts overlain by boxy anticlines related to the flat-to-ramp detachment of the thrusts above the main south-dipping detachment (Bemis and Wallace, 2007). The northern-most range front of the foothills is defined by the scarp of a large monocline, interpreted as a fault-propagation or fault-bend fold based on the steep forelimb and gently dipping back limb (Bemis, 2004). North of the range front, the Japan Hills are interpreted to reflect a thrust wedge at depth, with the north flank of the hills being actively deformed by the northward propagation of the thrust wedge and the south flank being deformed above a north-dipping back thrust (Bemis et al., 2012). This pattern of faulting can be recognized throughout the apex of the convex arc that defines the foothills region, although to the east of the Japan Hills, the northernmost thrust is difficult to distinguish, which could be due to the lack of detailed geologic maps in this area. Figure 2.3 shows a compilation of geologic map data, along with known faults and folds within the study area.

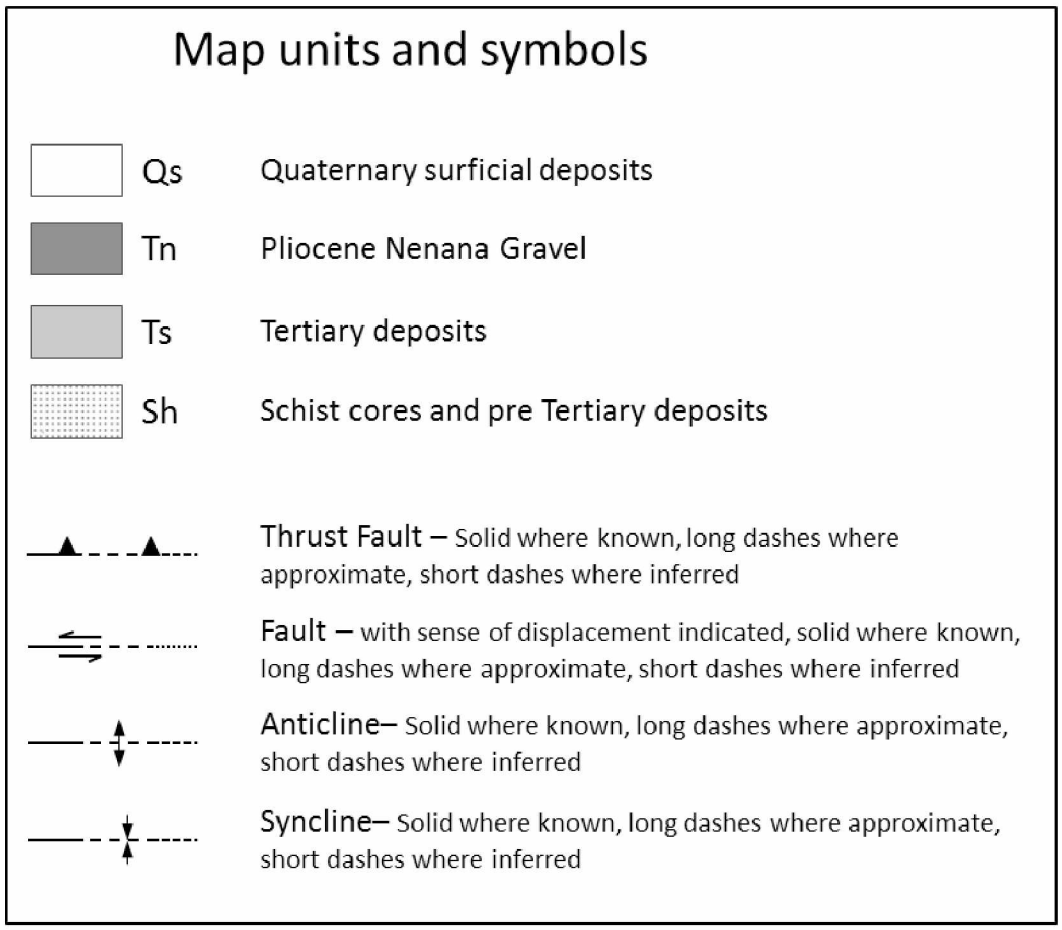

Figure 2.3 Revised Generalized Geologic Map of the Northern Foothills of the Alaska Range. Geology is based on Bemis (2004). Faults and anticlines are based on Bemis (2004), Bemis et al. (2012), and Bemis, written comm., 2012. Map covers area outlined in figure 2.1.

2.4 Regional Geomorphologic Analysis

The geomorphology in a mountainous region carries information about the landscape's response to recent tectonic movements in the area. To extract this information, it is, however, necessary to isolate the tectonic signal from the other factors that influence geomorphology, such as variations in resistance to erosion of different rock units and river and glacier response to climatic changes. Several geomorphic indices were applied to highlight the tectonic component of the local geomorphology and assess where recent neotectonic deformation has occurred. This was accomplished by using both quantitative and qualitative indices. Examples of qualitative analyses that have been previously completed in the area are mapping river terrace profiles and mapping changes in longitudinal river profiles (Bemis, 2004, 2010; Bemis and Wallace, 2007; Lesh, 2002; Lesh and Ridgway, 2007). The quantitative analysis using the stream length-gradient index was conducted by Lesh and Ridgway (2007).

2.4.1 Longitudinal River Profiles

The longitudinal river profile is the measurement of the elevation of the river along its course and is an indicator of the balance between erosion and uplift rates as well as other factors that can also influence the profile such as discharge, rock erodibility, and base-level change (Keller and Pinter, 2002; Perez-Pena et al., 2010). The ideal profile of a river (Figure 2.4) can be described as a negative logarithmic function (Hack, 1973).

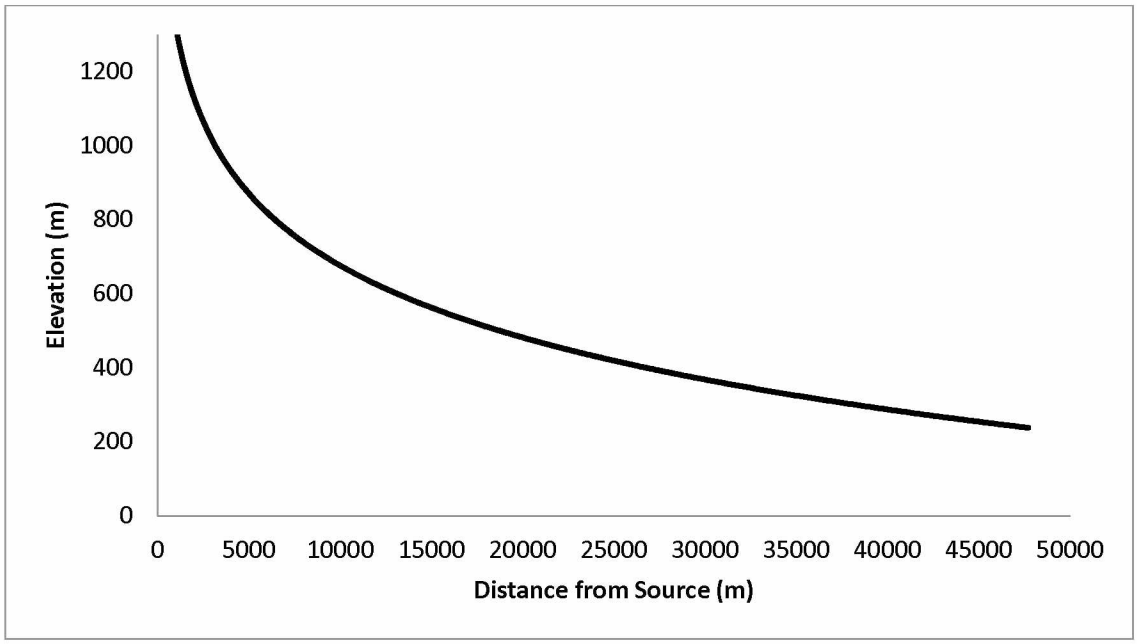

Figure 2.4 Ideal Elevation Profile of a River. Longitudinal elevation profile of an ideal river modeled by a negative logarithmic curve.

The longitudinal profiles of rivers can indicate where tectonic uplift exceeds erosion in an area by deflecting the ideal river profile with either a “bump” or a “knickpoint” (Figure 2.5) (Larue, 2010). While such profile deflections may also be caused by different rock types having different resistances to erosion, this area offered evidence that the longitudinal profiles of these rivers are minimally affected by rock type (Bemis, 2004; Bemis and Wallace, 2007; Lesh and Ridgway, 2007). This suggests that in the study area, deflections from ideal river profiles may be used to identify areas of active tectonics, such as a faults or growing folds (Seeber and Gornitz, 1983).

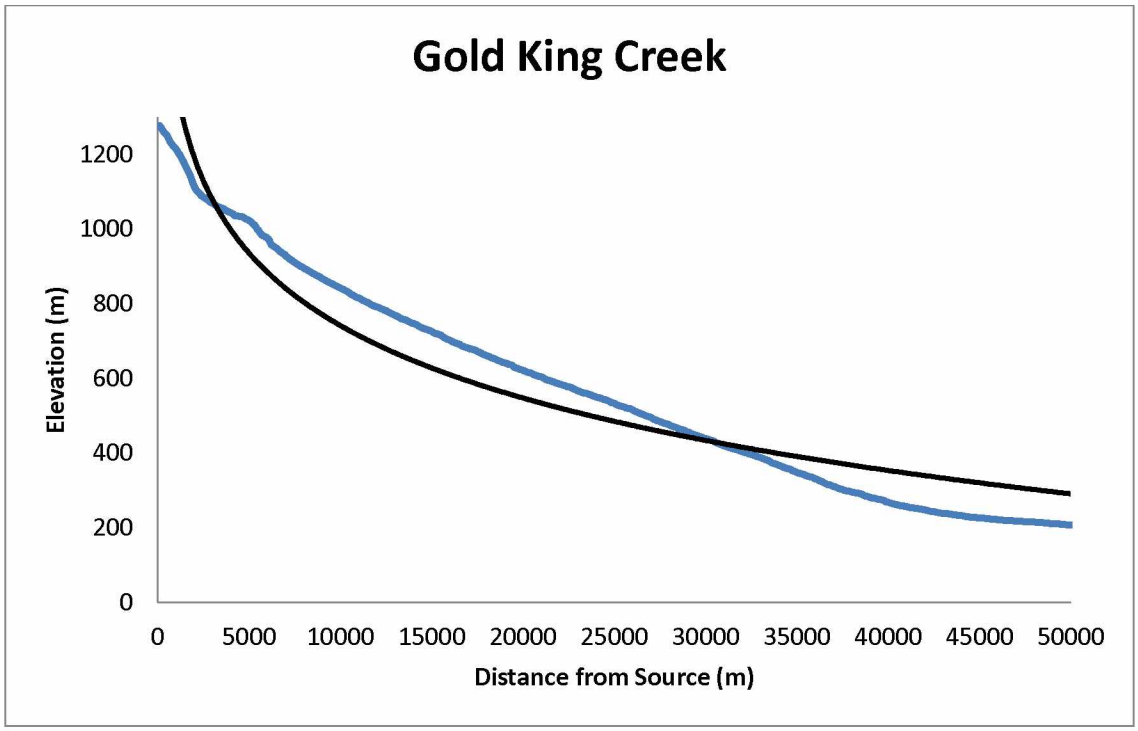

Figure 2.5 River Profile Exhibiting a Tectonic "bump." Gold King Creek profile, blue line, showing deviations from the ideal profile, black line. Deviations include a "bump" in the data near the headwaters of the stream and an anomalously high linear gradient that ends around 40,000 meters from the source.

2.4.2 Stream Length-Gradient Index

Hack (1973) first derived the Stream Length Gradient Index (SL Index), a quantitative geomorphic index, by taking the change in elevation of the measured reach ($\boldsymbol{\Delta H}$), which is the section of river being measured along the profile, divided by the length of that given reach ($\boldsymbol{\Delta L}$) and then multiplying that number by the length of the stream from halfway up the measured reach to the stream head ($\boldsymbol{L}$).

$$\boldsymbol{SL} = (\boldsymbol{\Delta H} / \boldsymbol{\Delta L})\boldsymbol{L} \qquad \textbf{(1)}$$

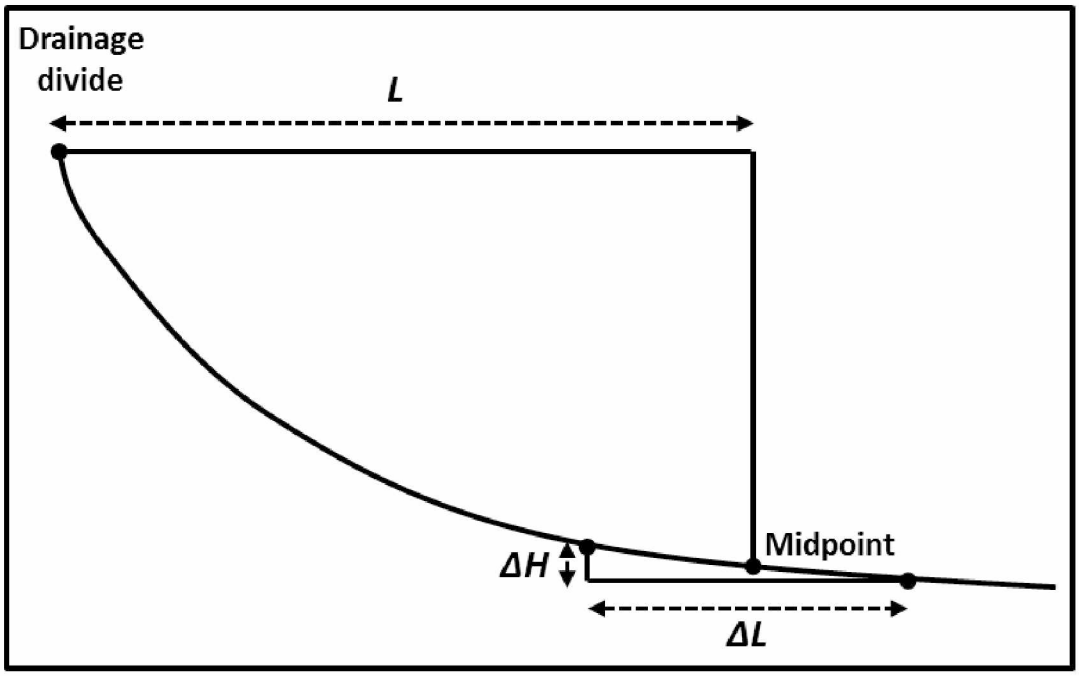

Figure 2.6. Graphical Representation of Stream Length-Gradient Index. Measurement of the SL Index along a stream profile (After Font et al., 2010).

The SL Index is used to describe the gradient change of a stream along a specific segment of its channel and is sensitive to changes in rock resistance and tectonic uplift (Hack, 1973). Where the rocks in a study area consist of poorly consolidated terrestrial sediments and easily eroded metamorphic rocks, anomalies in the SL Index can be attributed to tectonic uplift, and not to rock resistance (Bemis, 2004). When a stream travels over an area of active tectonic uplift the SL Index will reflect this with an anomalously high value. Where anomalously high SL Indices can be mapped over an area, they may correlate with active faults or growing anticlines (Font et al., 2010). Issues can arise with the SL Index because it is sensitive to the length and order of a river, which makes comparing rivers of different lengths difficult. The order of a river is

determined by its number of tributaries. In general, as a river gets longer, the number of tributaries increases, and the order of the river increases. If there are no tributaries the stream is considered of the first order. Two first order streams meet to form a second order stream, and so on and so forth. As the order and length of a river increases so does the power that the river has to erode its stream bed. It has been found that the SL Index is more accurate on first order streams unless the data is normalized, usually by dividing the SL Index by *K,* which is the slope of the ideal profile (Perez-Pena et al., 2010). Because the SL Index is calculated from the longitudinal profiles of rivers they are inherently correlated. Figure 2.7 plots the correlation between the longitudinal river profile (blue line), and the SL Index (red line). It is seen that the spikes in the SL Index plot are associated with the deviation of the longitudinal profile from its ideal shape (black line).

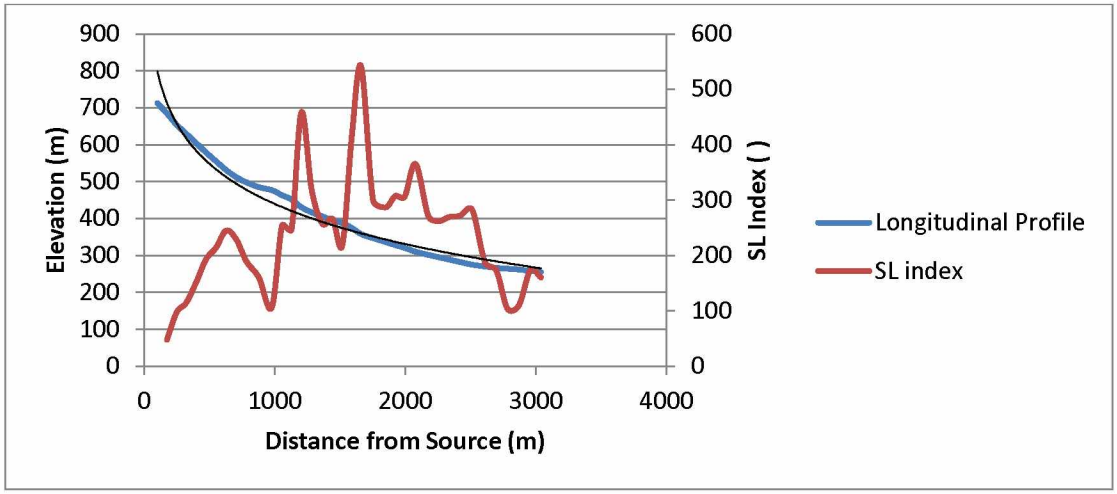

Figure 2.7 Correlation between Longitudinal Profile and SL Index. Where the longitudinal profile (blue line) deviates from its ideal profile (black line), the SL Index values (red line) spike anomalously.

2.4.3 Previous Geomorphic Analysis of the Region of Interest

Lesh (2002) studied twenty-five rivers that flow north out of the Alaska Range using the available National Elevation Dataset (NED) DEM's and attempted to mitigate DEM errors using a 100 meter running average. From his analysis of the longitudinal profiles, Lesh (2002) determined areas of basin subsidence and tectonic deformation (Lesh, 2002; Lesh and Ridgway, 2007). Bemis (2004) measured longitudinal river profiles using three different data sets: real time Global Positioning System (GPS) surveys, United States Geologic Survey (USGS) NED DEM's and USGS 1:63,360 scale topographic maps. Bemis (2004) showed that using a real time differential GPS provided the most precise elevation values, although the method is impractical to apply over a large study area due to the remoteness of the area and the large amount of time it would take to map the rivers. He found that using the USGS 1:63,360 topographic maps was time efficient and reduced the small-scale errors in the USGS NED DEM's (Bemis, 2004; Bemis and Wallace, 2007). Both Lesh (2002) and Bemis (2004) found that all streams that flowed north through the foothills deviated from the ideal logarithmic shape, without significant effect of rock type, thus indicating ongoing tectonic movement throughout the area.

Lesh and Ridgway (2007) compiled an SL index map of the northern foothills of the Alaska Range. Their analysis was based on the 60 meter USGS NED DEM's that spanned the region and included 25 of the larger rivers that go through the area. Because the SL

index can be skewed in the longer reaches of a river, they normalized the data using the slope of the ideal profile for the river (Lesh and Ridgway, 2007). They found that the Tanana Basin north of the foothills is being actively deformed by the growth of east trending anticlines. Concurrently, the area east of the foothills is being deformed by a combination of both thrust and strike-slip faulting. Since their conclusions were based on the twenty-five larger rivers that span such a large area, smaller-scale deformation was lost in the coarse resolution of the study.

3.0 Relevant Remote Sensing Theory

Remote sensing in the field of geology has been used since the advent of the camera. Image interpreters in the past were limited by the course resolution of the sensors and the reliability of the platform the sensor was mounted on (Lillesand et al., 2008). In more recent years, the platforms have become more reliable, and both airborne and spaceborne sensors have improved dramatically in the optical as well as in the microwave wavelengths. In addition to improvements in sensor technology, new processing methods have contributed to recent major advances in the quality of geophysical information that can be retrieved from remote sensing data.

3.1 Wavelength and the Electromagnetic Spectrum

Remote sensing is based on the principals of electromagnetic (EM) radiation and how this energy propagates through the atmosphere and interacts with objects on the ground. EM radiation travels in the form of two orthogonal waves moving at right angles to each other, with one being an electrical component and the other a magnetic component. The radiation used by a sensor can be described by the signals amplitude (A), wavelength (λ), and polarization. All EM waves can be described using these features. The signal's wavelength is often also expressed in terms of the frequency with which the EM wave oscillates when it propagates through space at the speed of light (c). Frequency is given by $f = c / \lambda$ and is measured in Hertz. The electromagnetic spectrum is

the range of wavelengths/frequencies that can be observed for EM radiation, and ranges from very high frequency waves such as Gamma Rays to very low frequency waves such as radio waves. The three main regions of the electromagnetic spectrum that are used for Earth observation are the optical, infrared and microwave regions.

3.2 Properties of Optical Remote Sensing

Optical sensors make use of visible, near infrared, short-wave infrared regions of the electromagnetic spectrum to form an image of the Earth's surface by detecting solar radiation reflected from targets on the ground (Lillesand et al., 2008). Within these regions there are many areas where the transmissivity of the atmosphere is low. In these parts of the EM spectrum, atmospheric molecules interfere with the EM wave and reduce the quality of the observed information. Figure 3.1 shows atmospheric transmissivity at visible, infrared and thermal wavelengths. Optical data is collected passively, which means that the sensor collects energy that originates from an external source (mostly the sun) that is not the sensor and was reflected off the Earth and to the sensor. Because of this passivity, optical sensors are designed so the wavelengths that are being collected are located in the areas of maximum transmission through the atmosphere. This can be seen in Figure 3.1, with examples of band locations for the ASTER and Landsat satellites. The blue line in Figure 3.1 shows a smoothed percentage of water vapor absorption across the spectrum, which is very high across the visible,

near infrared and short-wave infrared regions, which means that the sensor cannot "see" though clouds and is therefore weather dependent.

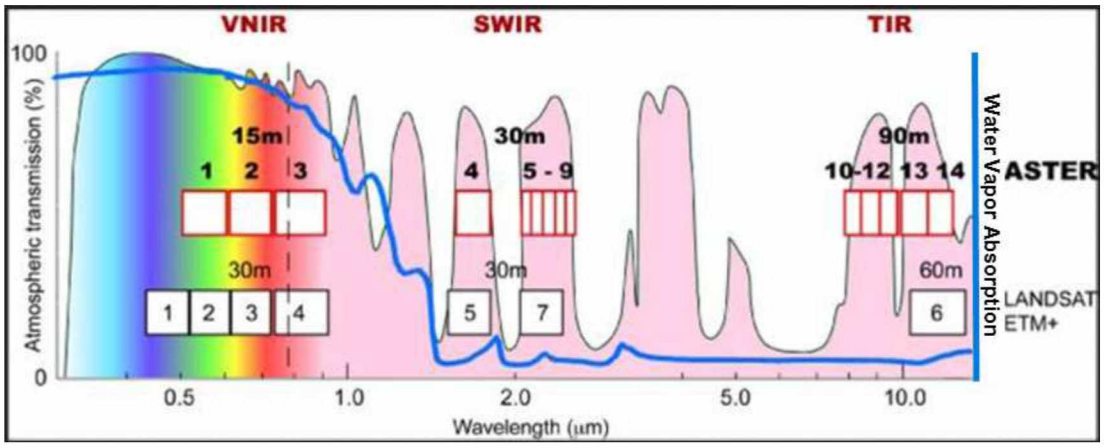

Figure 3.1 Atmospheric Opacity, Optical Region. Diagram of atmospheric opacity over the visible and near infrared portion of the electromagnetic spectrum. Optical sensors are designed with bands located in the spectrum where the transmission is more, aka in the visible region, (blue, green, and red), the Near Infrared, Shortwave Infrared. ASTER and Landsat ETM+ bands are shown here. (http://asterweb.jpl.nasa.gov/)

Optical data inherently tells the user the chemical makeup of what is being observed, such as the amount of chlorophyll in vegetation or the mineralogy of bare rock. So when there is a change in the atmosphere or ground cover between scenes, comparing features that should be static such as rocks that are bare in one scene and covered with snow or vegetation the in the next is virtually impossible. Because of the variation that can found from season to season and day to day in optical data, radar sensors are better suited for observing static objects, while optical sensors are better used for tracking change.

3.3 Properties of SAR Remote Sensing Data

Synthetic Aperture Radar or SAR satellite remote sensing uses the microwave portion of the EM spectrum, which is found in the millimeter to meter-sized wavelength range. Figure 3.2 shows that, as the wavelengths of the EM signals become longer, transmissivity through the atmosphere increases until the signal is no longer affected by atmospheric constituents.

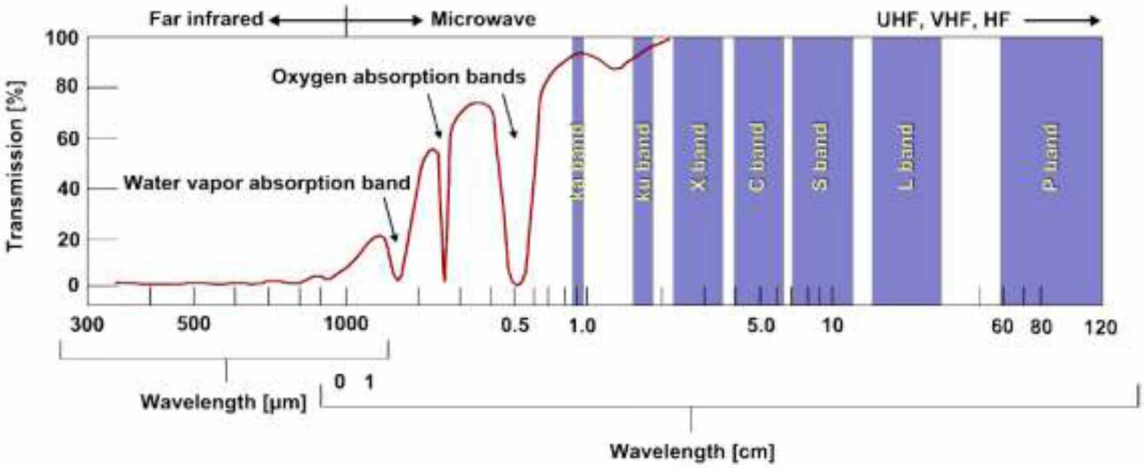

Figure 3.2 Atmospheric Transmissivity for the Microwave Part of the EM Spectrum. The atmospheric transmissivity is shown as red line. The main frequency bands used for microwave remote sensing are labeled. Prominent absorption lines for atmospheric gases are highlighted. Source: Gens, 2008

SARs are active systems that send out pulses of energy and measure the amount of energy that gets reflected and returned to the sensor. Due to its active nature combined with the high transmissivity of the atmosphere for microwave signals, SAR data can be collected during day and night and independent of weather conditions.

Due to the specifics of the image formation process, SAR satellites always observe the Earth at an oblique, side-looking angle, and most look to the right (see Figure 3.3). As the sensor travels along its flight path (referred to as the "azimuth" direction) and looks to the right (range direction), an area of the ground is imaged. The area that is imaged by the sensor at the time of acquisition is called the image "swath". The swath extends from the near range edge (the closest point to nadir that is imaged by the system) to the far range edge of the SAR antenna footprint. The distance from the near range to the far range edge is called "swath width". The image is originally in the "slant range" geometry in which surface elements are sorted by their respective range to the sensor. The slant range image can be projected into a ground range image using information about the observation geometry. One relevant geometry parameter is the look angle, which is defined as the angle between nadir and the off-nadir orientation of the SAR antenna.

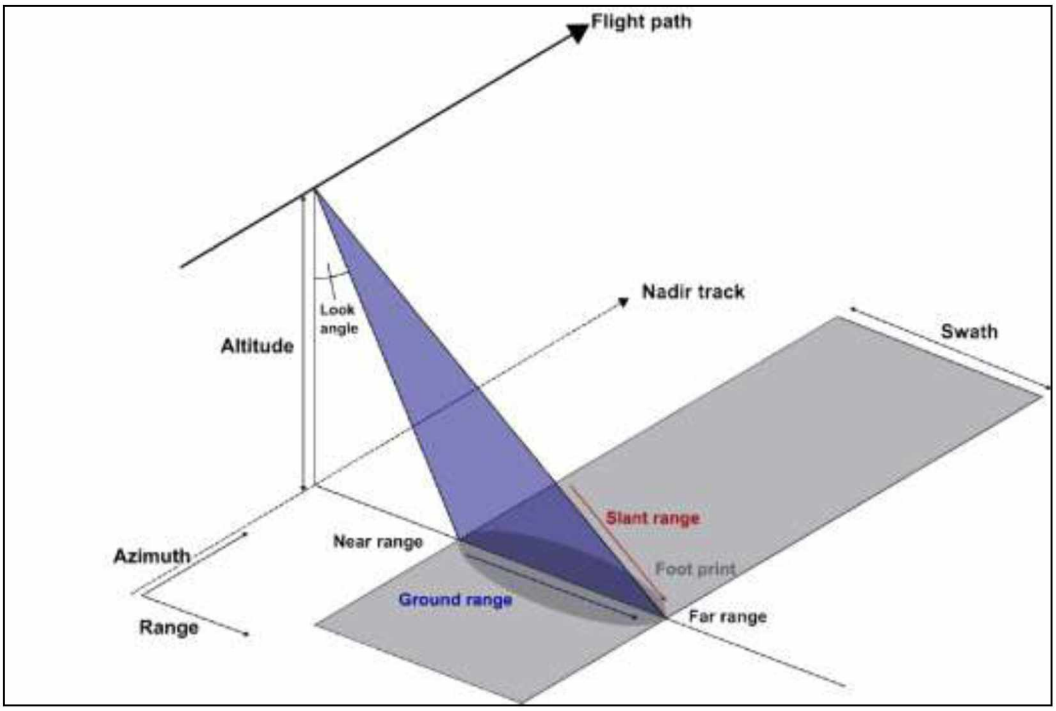

Figure 3.3 Viewing Geometry of a SAR Sensor. Shown here are the elements of the viewing geometry of the SAR sensor. The purple area is where the sensor "sees" at any given point in time and the grey shaded zone is the area of the earth that was acquired over a given period of time. Source: Gens, 2008

3.3.1 Geometric Artifacts

As a SAR observes the ground in a side-looking geometry, certain geometric distortions emerge that are correlated with surface topography. We generally discriminate three interrelated geometric artifacts that are regularly found in side-looking SAR images including (1) foreshortening, (2) layover, and (3) radar shadow. The magnitude of these artifacts increases with local surface slopes and is therefore directly linked to the local topography.

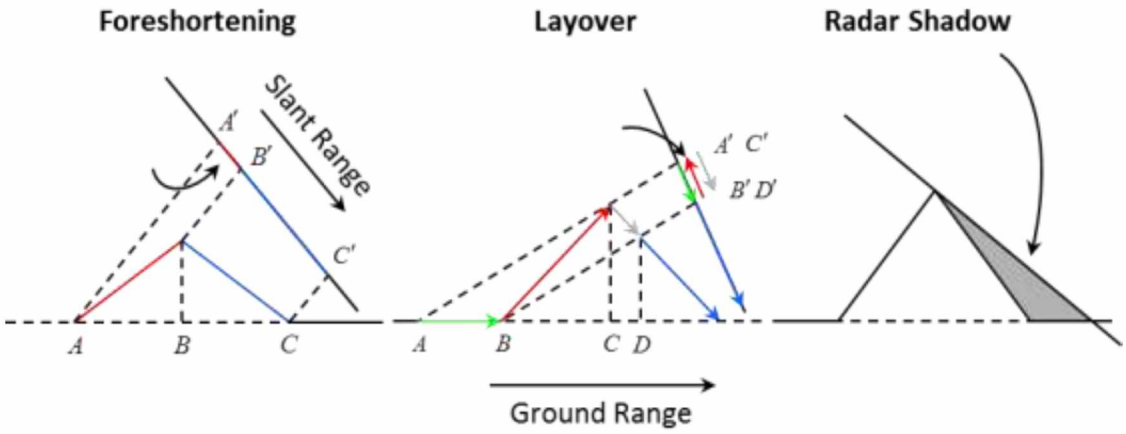

Figure 3.4 Schematic of Geometric Artifacts of SAR. The type of geometric artifact that can occur in a SAR image is dependent on sensor look angle, slope and mountain height. Source: Meyer, 2009.

Geometric interpretations of foreshortening, layover, and radar shadow are shown in Figure 3.4, which shows how topographic features get distorted when they are projected into the slant range geometry by the SAR image acquisition process.

Foreshortening appears in places where the local surface slope (the inclination of a sloped surface measured from the horizontal) is close to, but smaller than the look angle of the radar system. In foreshortened areas, sensor-facing mountain slopes get foreshortened, giving the mountains the appearance of "leaning" towards the sensor (see Figure 3.5a for a real-data example). This is due to the fact that, on steep slopes that face the sensor, the signal at the base of the slope returns to the sensor at nearly the same time as the signal from the top, effectively pulling the tops of the mountains towards the base. Due to the dependence on the look angle of the sensor, foreshortening is more pronounced in near-range and diminishes towards the far-range

edge of the image. If the topography of the imaged area is known, foreshortening can be mitigated through a process called terrain correction (see Section 3.3.2).

If the local surface slopes exceed the look angle of the sensor, foreshortening turns into **layover**. Here, the return signal from the top of the mountain will reach the sensor before the signal from the bottom of the mountain, overwriting any information that may have come back to the sensor from the base of the mountain (see Figure 3.5b for an example). The effect of layover cannot be corrected by terrain correction and the data "trapped" under the top of the mountain is lost. To fill the data hole in the affected area would be to find data from a different acquisition made with a different look angle. Similarly to foreshortening, the likelihood of encountering layover increases with increasing surface slopes and is higher in near range than far range.

A third related imaging effect is **radar shadow**, which appears when the absolute value of slopes facing away from the sensor exceeds the sensor look angle. In these cases, no incoming microwave radiation hits certain areas behind the mountain top, causing those areas to remain empty in the image. Compared to foreshortening and layover, shadow has an opposite look angle dependence and worsens towards the far-range edge of the image.

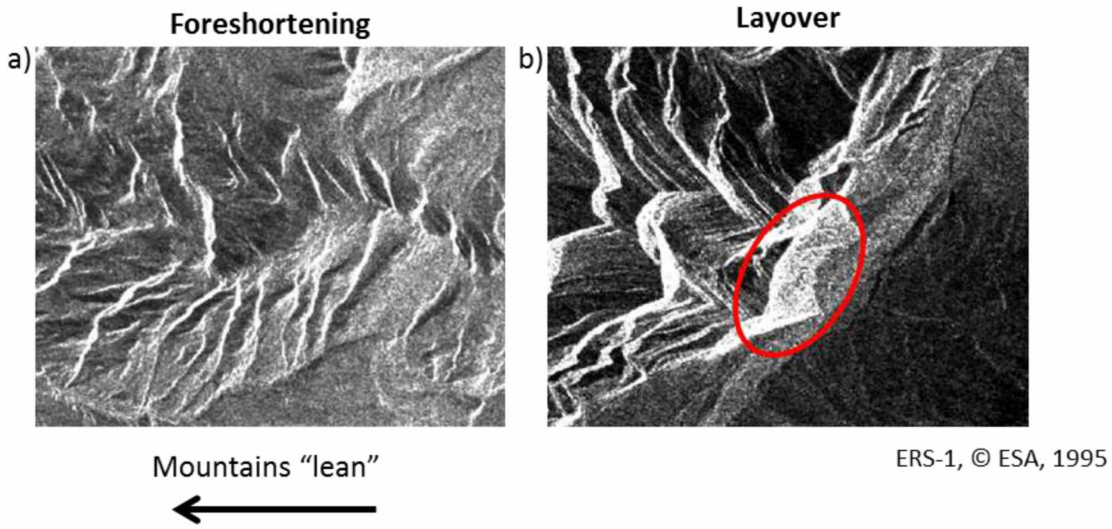

Figure 3.5 Examples of Geometric Artifacts. These SAR images show how (a) foreshortening and (b) layover can affect the data in an area. The red circle on the layover image shows the mountain top leaning over a river effectively obscuring any data 'under' the mountain.

Similar to layover, radar shadow effects can only be corrected if images with different look angles or viewing geometries are combined in order to fill in the shadowed areas. If the observation geometry and the local surface topography are known, the extent of shadow and layover areas can be calculated and converted into masks. These layover and shadow masks can be used to exclude areas with unreliable radar response from further data interpretation and processing.

The SAR data used in this study was exclusively acquired in right-looking geometry with a mid-range look angle of 23.1 degrees. The steep look angle causes layover and foreshortening to be prevalent in the images with layover occurring in most of the high mountains in the southern half of the study area.

3.3.2 Terrain Correction

Terrain correction of side-looking SAR data can entail two steps: (1) geometric terrain correction, which is converting the image from the side-looking radar geometry into a geometrically corrected image, and (2) radiometric terrain correction which additionally corrects for topography-related shading effects that bias the signal intensity that is received per pixel.

Geometric Terrain Correction: Figure 3.6 shows an example of the effects of geometric terrain correction on SAR image data by presenting (a) a non-terrain corrected image on the top and (b) a geometrically terrain corrected image in the middle. A DEM of sufficient resolution and accuracy is necessary to transform every slant-range pixel into its corrected geometric space. For detailed information on processing steps and equations used for geometric terrain correction see "Terrain influences in SAR backscatter and attempts to their correction," by Bayer et al., 1991.

Although, after geometric terrain correction, the image is corrected geometrically, there are still radiometric distortions that are caused by the side-looking observation geometry. Sensor-facing slopes of the topography have a brighter backscatter (white areas in images (a) and (b) in figure 3.6) then the slopes that face away from the sensor. To correct for this distortion, **radiometric terrain correction (RTC)** is applied. RTC is removing the distortions of received backscatter amplitudes that are introduced by geometric effects on sloped surfaces. On sensor-facing slopes, the surface area that is

projected into one pixel increases with slope angle. The combination of a larger number of surface responses per pixel results in an overinflated image brightness at sensor-facing slopes. Such geometry-related radiometric distortions appear in all areas where the surface slope is different from zero. These artifacts can be corrected through RTC if topographic information of sufficient quality is available. After RTC the image looks flattened and the backscatter is a representation of the ground surface without the effect of topography. This is illustrated in figure 3.6 (c). This is an important step to take in terrain-dominated areas so that a classification can be based on physical parameters and not geometric artifacts manifesting themselves in the SAR data. Examples of radiometric artifacts have been seen in studies that classify vegetation using SAR data. Without RTC the vegetation on the side of the hill facing the sensor is classified differently from vegetation on the opposite slope. When radiometric terrain correction is applied, the classification is improved (Atwood et al., 2012). For detailed information on processing steps and equations used for radiometric terrain correction the reader is referred to "Flattening Gamma: Radiometric Terrain Correction for SAR Imagery," by David Small (2011).

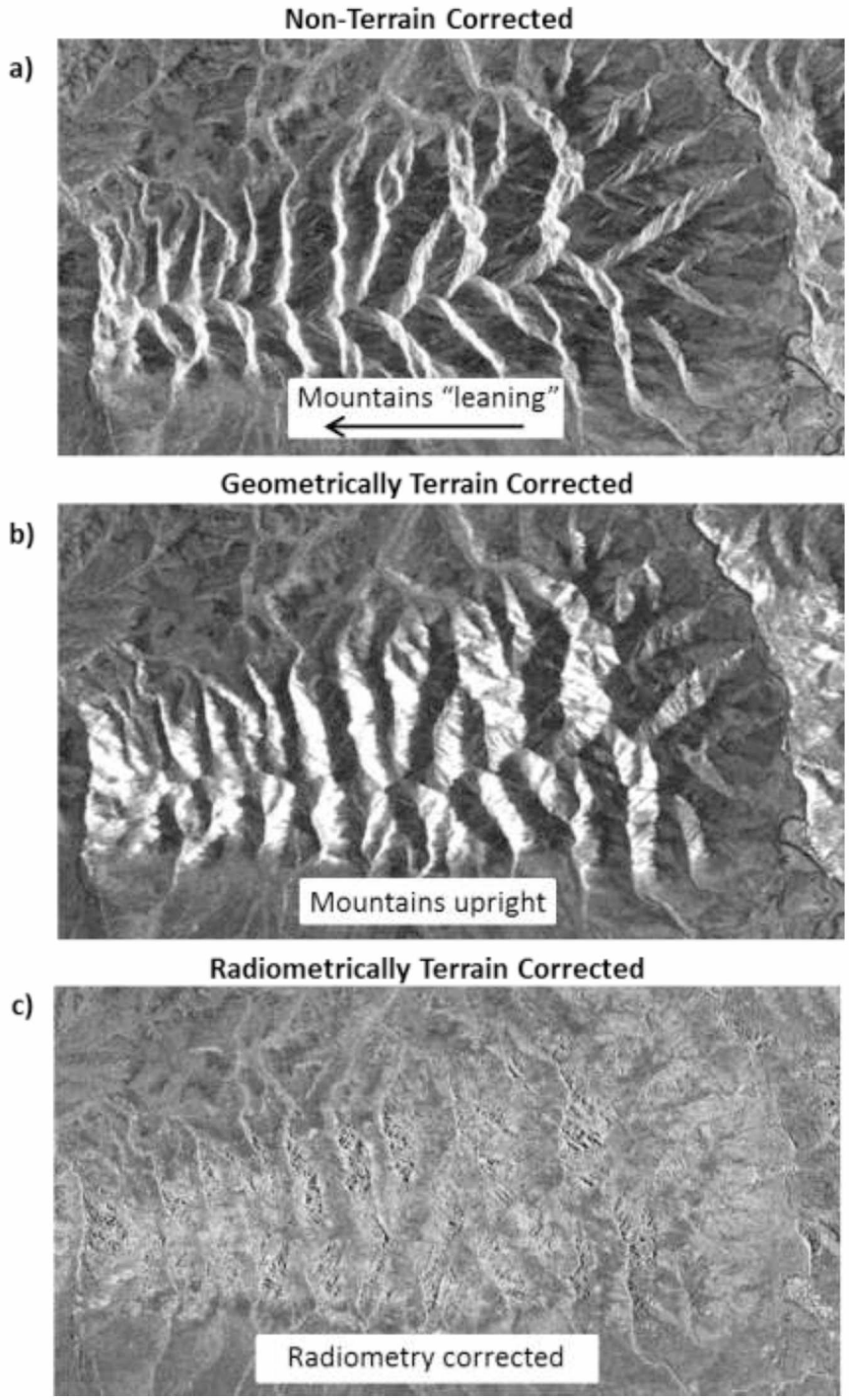

Figure 3.6 Effects of Terrain Correction. Image (a) is non-terrain corrected and the mountains appear to "lean" towards sensor. Image (b) is terrain corrected and the mountains are now geometrically correct in ground range and "stand upright". Image (c) has been radiometrically terrain corrected; the topographic-related pixel over-brightness is corrected leaving a non-distorted interpretation of the surface.

3.3.3 Observational Parameters of a SAR System

In active microwave remote sensing, the waveform used for sensing can be created, sent and received in different configurations depending on the platform and intended use of the data. One main signal parameter is the orientation of the plain in which the electric field of the EM signal is oscillating. This orientation is referred to as the "polarization" of the signal. Most SAR sensors transmit and receive linearly polarized signals with the EM waves oscillating in horizontal or vertical orientation, creating four different imaging scenarios for linearly polarized SAR systems as depicted in Figure 3.7.

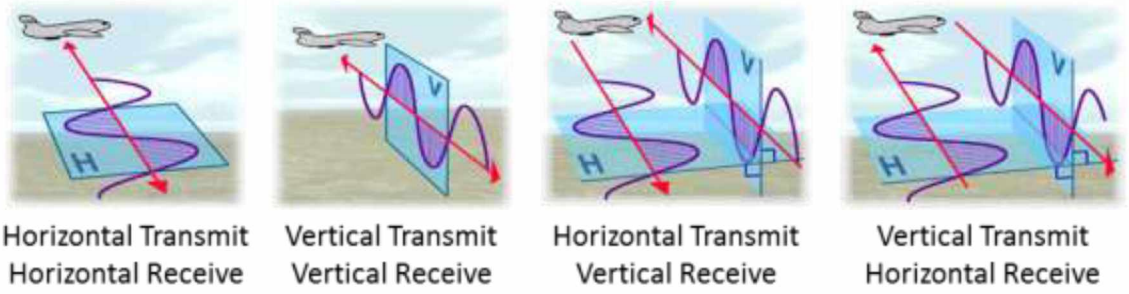

Figure 3.7 Signal Polarizations. SAR sensors can transmit and receive signals in horizontally or vertically polarization, resulting in the four acquisition scenarios depicted above. Source: Meyer, 2009.

Not all SAR systems offer the full set of acquisition options that is depicted in Figure 3.7. A single-pol sensor only transmits and receives waves in a single configuration, such as vertical transmit, vertical receive (VV) or horizontal transmit, horizontal receive (HH). Dual-pol configurations typically provide the combinations VV and VH, HH and HV, or HH

and VV. A quad-pol system provides all the possible linear polarizations including HH, VV, HV, and VH. As part of each of these configurations the SAR wave carries two pieces of information, the amplitude and the phase of the returning signal. The amplitude is the energy of the returned wave and the phase is the measurement of the leftover fraction of the wave at the time it returns to the sensor. The interaction of the wave with objects on the ground affects the returning signal in a distinctive fashion, with different objects rotating, reflecting, or diffusing the wave differently.

3.3.4 Main SAR Scattering Principles

When the signal transmitted by the radar sensor hits the ground, a part of the signal gets scattered back towards the sensor. The amount of backscattered signal depends on the surface's dielectric properties and its geometric shape. The backscattered response can be described as a combination of four main interactions between the radar signal and the surface. These interactions are schematically illustrated in Figure 3.8 and are double bounce, volume or diffuse, bragg, and specular scattering.

Double bounce scattering (Figure 3.8 bottom left) models the scattering off dihedral reflectors, such as tree trunks, sharp topographic rises, or man-made structures (buildings, walls or pipelines, etc.). The wave hits the ground, gets scattered up to the reflector and then bounces back to the sensor. The return from a double bounce reflector can be very strong if the involved surfaces scatter a large percentage of the

incoming energy in an oriented manner. In a natural environment double bounce scatterers will usually represent tree trunks in a forest. Double bounce scattering is more efficient in HH polarization than in VV polarization and can be identified by analyzing scattering ratios between HH and VV data.

Volume scattering (Figure 3.8 bottom right) models the interaction of microwave signals with scatterers that are arranged in a three-dimensional voluminous space. Typical bodies that act as volume scatterers are forest canopies, dry sand, or dry snow. The microwave signal will penetrate into the volume, bounce around inside, and only a portion of this wave is returned to the sensor. The sand and snow have to be dry for this mechanism to occur because an EM wave can only travel in the void spaces between the particles of snow and sand. If water fills that void the return will not act as a volume scatter. Volume scattering leads to a depolarization of the transmitted signal. This means that some part of a horizontally polarized signal will be returning to the sensor as a vertically polarized signal. Hence, if full-pol data is available, volume scatterers will have strong responses in the HV and VH polarization (Cui et al., 2010).

Specular and Bragg scattering are also known as a single bounce scattering processes. Here, the backscattered response is the product of only one scattering event. Specular scattering (Figure 3.8 top left) is what happens when the wave interacts with a smooth surface such as water or pavement and reflects away with little or no return to the sensor. Bragg scattering (Figure 3.8 top right) is when the wave interacts with a rough

surface. A rough surface will have relative height differences greater than one quarter the wavelength of the waveform. Any height difference less than that is considered smooth and will exhibit specular scattering. The energy of the returned signal depends on the level of surface roughness and incidence angle (Woodhouse, 2006) as depicted in Figure 3.9. Bragg scattering is more efficient in VV polarization than in HH polarization and can be identified by analyzing ratios between VV and HH channels. Of all the scattering mechanisms this represents the physical properties of the Earth's surface best and is the most important when describing the surface geology of an area.

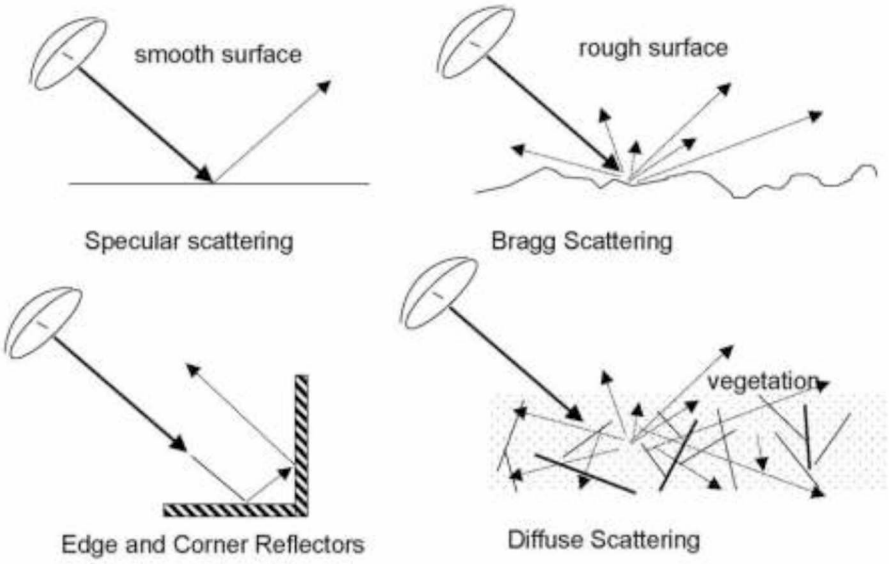

Figure 3.8 Backscatter Differentiation. The four different ways that the radar signal can be scattered are Specular Scatter, Bragg Scatter, Dipole or Edge Scatter and Diffuse Scattering. Source: Meyer, 2009.

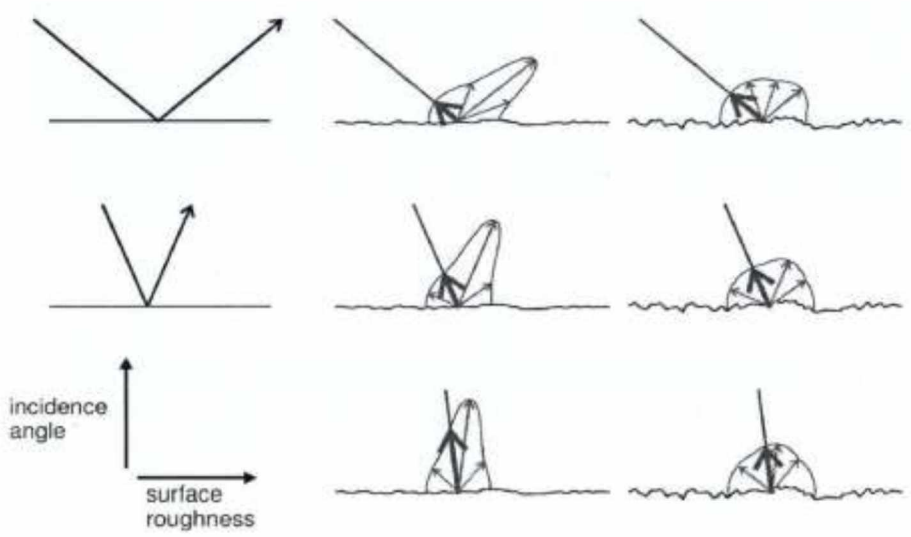

Figure 3.9 Effects of Surface Roughness and Incidence Angle. Specular reflection occurs on smooth surfaces, while Bragg scattering occurs on the rough surfaces, with the amount of energy returning to the sensor dependent on the relative roughness of the surface. Source: Woodhouse, 2006.

4.0 Remote Sensing and Ancillary Data

Data from three different sources representing two types of remote sensing systems were reviewed for use in this study. Data from Radar and Optical sensors were to be combined to describe the observed surface in three dimensions and analyze its geology. The radar data used in this study is SAR data collected by the Japanese Aerospace Exploration Agency's (JAXA) Advanced Land Observing Satellite (ALOS) Phased Array-type Synthetic Aperture Radar (PALSAR) sensor, as well as the European Space Agency's (ESA) European Remote-sensing Satellite (ERS) 1 & 2 SAR satellites. The optical data is from the National Aeronautics and Space Administration's (NASA) Landsat 5 Thematic Mapper (TM) and Landsat 7 Enhanced Thematic Mapper Plus (ETM+), along with JAXA ALOS Advanced Visible and Near Infrared Radiometer type 2 (AVNIR-2) and its Panchromatic Remote-sensing Instrument for Stereo Mapping (PRISM).

4.1 Radar Data

The ALOS PALSAR instrument is a Phased Array type L-band SAR sensor, which is an active microwave sensor that can collect data day or night with little to no atmospheric interference. PALSAR has three operating modes: Fine beam (single- and dual-polarized), ScanSAR and Polarimetric. The ScanSAR mode has a spatial resolution of 100 meters, a resolution that is deemed too coarse for this study. The fine beam mode has a resolution of 10 to 20 meters depending on the look angle and the polarimetric mode

that provides data at 30 meters resolution, both of which are suitable for the study (JAXA, 1997). The ERS-1 and ERS-2 satellites have a ground resolution of ~30 meters (ASF, 2013). The two ERS satellites are two identical sensors flown in an identical orbit. During most phases of their operational period, ERS-1 and ERS-2 observed the same area on ground with a time difference of only 24 hours. This is a convenient configuration for Interferometric SAR (InSAR) operations. InSAR data was used in this study to map topography in areas where topographic information from other sensors was scarce.

4.2 Optical Data

Optical data was intended to be used (i) for the creation of DEMs for the area of interest, (ii) for locating structural features that have an effect on the vegetative growth such as faults with imperceptible vertical offsets that can effect vegetation growth, and (iii) for determining river traces.

DEM generation was done using data from the ALOS PRISM sensor, a panchromatic instrument that spans the wavelengths 0.52 to 0.77 micrometers and has three optical sensors oriented in nadir, forward, and backward direction. PRISM produced imagery with a 2.5 meter resolution at nadir. Landsat-5 TM has seven spectral bands that range from the visible to the thermal infrared, with a resolution of 30 meters. Landsat-7 ETM+ also has seven spectral bands that are in the optical range from the visible to the

thermal infrared, with at resolution of 30 meters, and one panchromatic band with a 15 meter resolution. The AVNIR-2 sensor is comprised of four bands three in the visible range and one near infrared, with a resolution of 10 meters. Resolutions and wavelengths associated with the different sensors can be found in table 4.1.

4.3 Data availability

4.3.1 Remote Sensing Data

There is 100% coverage of the area in L-band SAR data from the JAXA ALOS satellite. These data come in several different configurations: high resolution single polarization, both ascending and descending; dual polarization, also ascending and descending; and full polarimetric data found only ascending. There is also 100% coverage of the area in C-band SAR data from both ESA's ERS-1 and ERS-2 satellites. Aside from the SAR data there is abundant optical data over the study area from ALOS AVNIR-2 and PRISM sensors, as well as NASA's Landsat-5 TM and Landsat-7 ETM+.

4.3.2 Ancillary Data

Topographic maps were utilized to extract river centerlines to be used in the Stream Length Index Gradient mapping. Geologic maps with well-defined geologic units and descriptions were used to train the classifier in the Polarimetric SAR classification of the

Nenana Gravel (see Section 5.3 for information on the data classification approach). Both the topographic maps and geologic maps were acquired from the Alaska State Division of Geological and Geophysical Surveys. Land cover classification data from the National Land Cover Database (NLCD) was used to mask out any area with vegetation that may interfere with the backscatter return of the SAR data, such as forested regions and wetlands.

Table 4.1- Satellite Data Availability. Satellite data available for use in this study, with sensor, band, wavelength and resolution information.

Satellite	Sensor/Type	Band/Mode	Wavelength/Frequency	Resolution
ALOS				
	PALSAR/SAR			
		L/FBS	23.6 cm/1.27 GHz	10 m
		L/FBD	23.6 cm/1.27 GHz	20 m
		L/PLR	23.6 cm/1.27 GHz	30 m
	AVNIR-2/Multispectral			
		Blue	0.42 - 0.50 µm	10 m
		Green	0.52 - 0.60 µm	10 m
		Red	0.61 - 0.69 µm	10 m
		Near Infrared	0.76 - 0.89 µm	10 m
	Prism/Multispectral			
		Panchromatic	0.52 - 0.77 µm	2.5 m
ERS-1&2				
	AMI/SAR			
		C - Band	5.6 cm/5.3GHz	30 m
Landsat-5				
	TM/Multispectral			
		Blue	0.45 - 0.52 µm	30 m
		Green	0.52 - 0.60 µm	30 m
		Red	0.63 - 0.69 µm	30 m
		Near Infrared	0.76 - 0.90 µm	30 m
		Shortwave Infrared	1.55 - 1.75 µm	30 m
		Shortwave Infrared	2.08 - 2.35 µm	30 m
Landsat-7				
	ETM/Multispectral			
		Blue	0.450 - 0.515 µm	30 m
		Green	0.525 - 0.605 µm	30 m
		Red	0.630 - 0.690 µm	30 m
		Near Infrared	0.775 - 0.900 µm	30 m
		Shortwave Infrared	1.550 - 1.750 µm	30 m
		Shortwave Infrared	2.090 - 2.35 µm	30 m
	Pan/Optical	Panchromatic	0.520 - 0.900 µm	15 m

4.4 Data Quality

4.4.1 Optical

While the area of interest was covered several times with high-resolution spaceborne multi-spectral images, persistent cloud coverage prevented the generation of a seamless, comprehensive, and blunder-free mosaic from these data. Multispectral data over an area is also affected by seasonal change in ground cover. The signal from vegetation is constantly changing throughout the year and in the winter, when leaves do not obscure the ground, a closed snow cover obstructs the underlying geology. Figure 4.1 shows the variability of ground reflectivity when imaged by optical sensors. Due to the groundcover and persistent cloud cover, multispectral satellite data was only used for visual interpretation and for the selection of training and validation sites to be used in SAR data classification procedures.

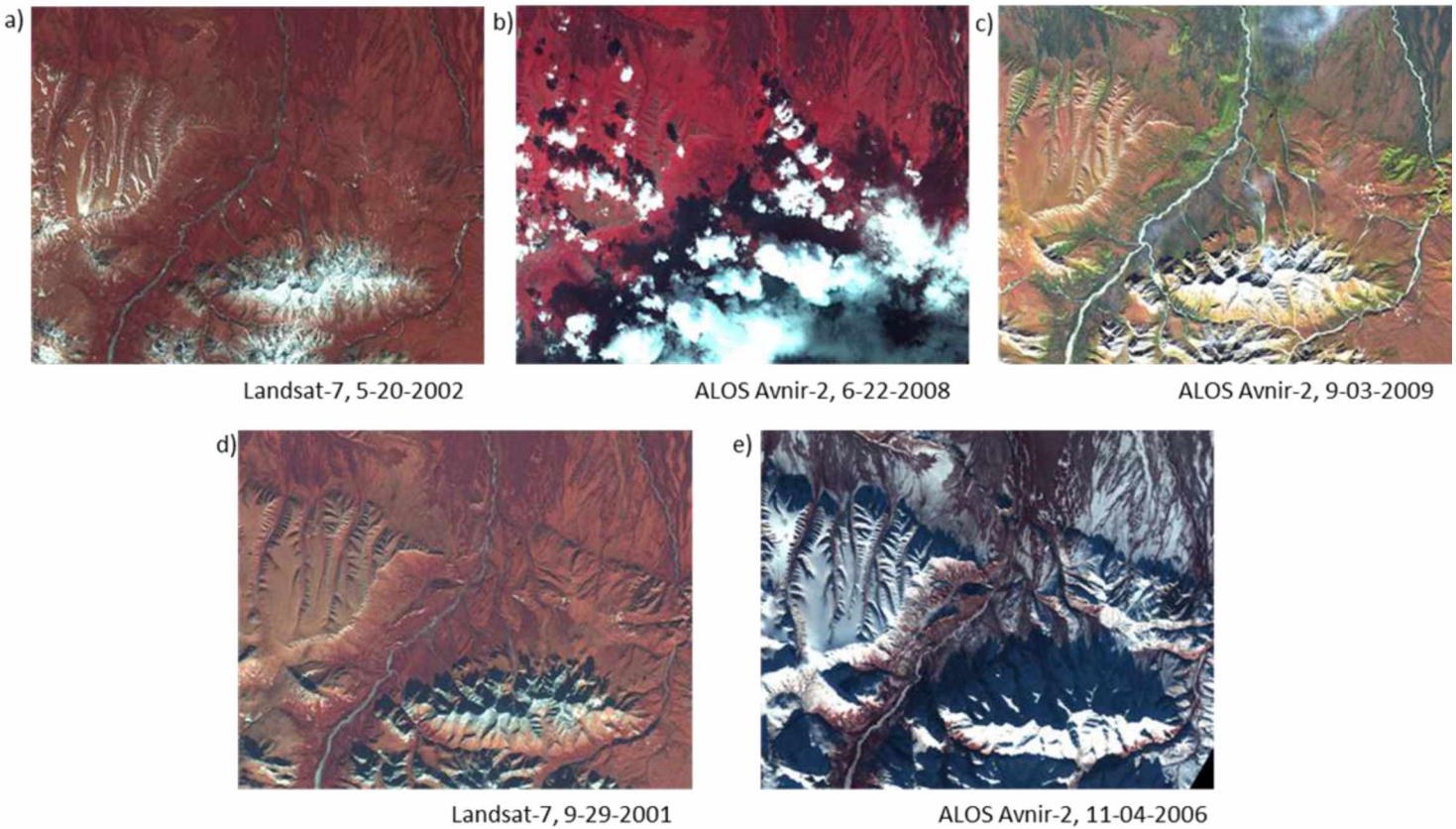

Figure 4.1 Optical Image Instability. Optical images over the study area showing clouds, snow cover and variation between acquisitions.

4.4.2 SAR

In comparison to the multispectral data, SAR data does not suffer from atmospheric effects and allows for regular imaging of the area of interest. The acquired full polarimetric ALOS PALSAR data provides data with higher consistency than the multispectral sensors. As will be shown later (see Figure 5.5), SAR observations acquired in similar seasons show radiometric consistency over many years, providing favorable conditions for geologic imaging. Figure 4.2 provides examples highlighting this temporal data consistency. The ability of longer wavelength SARs such as the L-band ALOS PALSAR sensor to penetrate shallow and sparse vegetation is an additional advantage that highlights the suitability of L-band SAR data for geologic mapping from images.

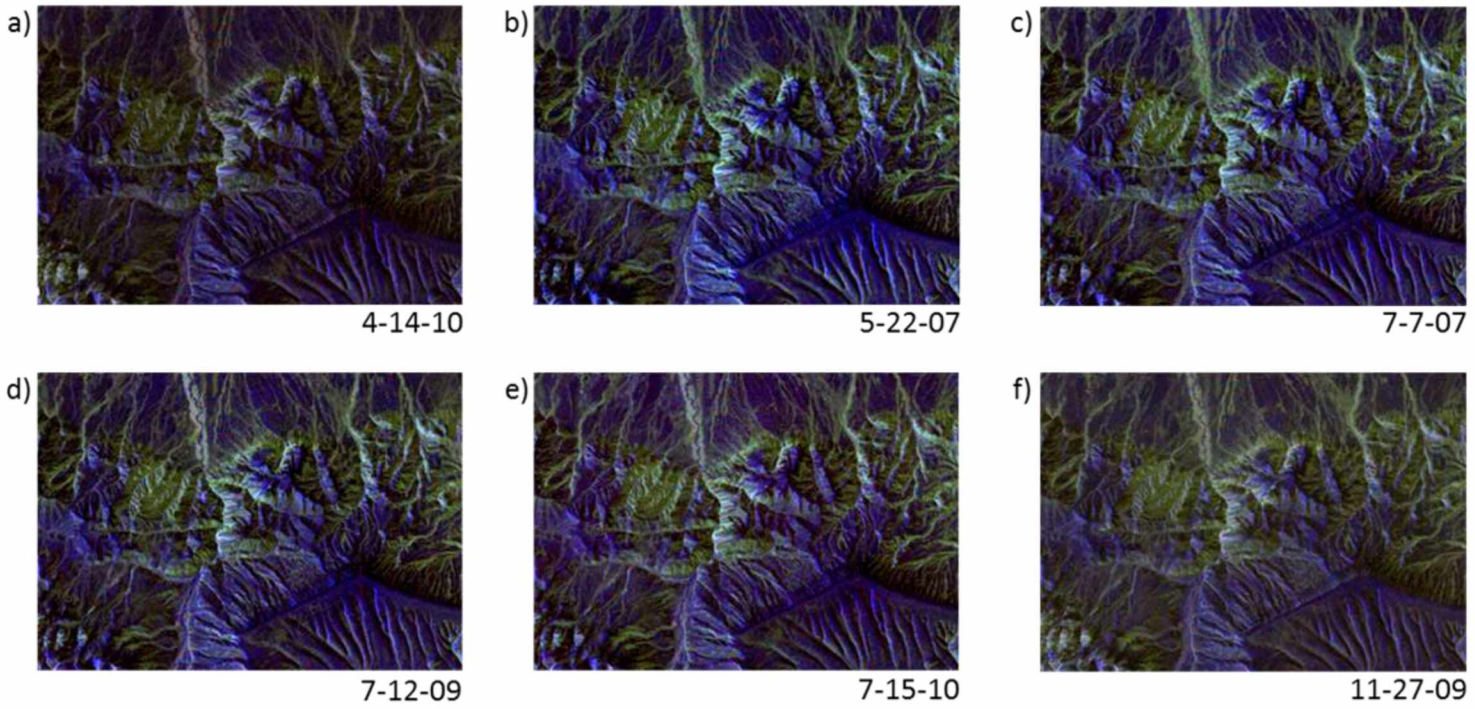

Figure 4.2 SAR Data Stability. Fully polarimetric data collected by the JAXA ALOS satellite, processed using the ASF Mapready tool into a Freeman-Durden polarimetric decomposition. The SAR data does not significantly change from year to year or in the winter months. This stability allows for the data to be mosaicked for use in the surficial geologic classification.

4.4.3 Ancillary Data

The topographic maps used for this project - Quadrangles Fairbanks A-1, A-2, A-3, A-4, A-5, B-1, B-2, B-3, B-4, B-5, C-3, C-4, C-2, Big Delta A-6, B-6, Healy D-1, D-2, D-3, D-4, D-5, C-6, Mt Hayes C-6, D-6 - , were produced between 1949 and 1951 with minor revisions added in the 1960's, 70's and 80's. The most comprehensive surficial geology maps of the area and the basis for the classification of the SAR data are the geologic maps that were first produced in 1970 by Clyde Wahrhaftig. These geologic and topographic maps use the 1927 North American Datum, with a Universal Transverse Mercator Zone 6 projection, which was transformed to WGS 1984 when the maps were imported into ArcMap for integration into the project. The NLCD land cover data is a Landsat derived dataset produced in 2001 that has a spatial resolution of 30 meters and covers the entire state of Alaska. NLCD data was downloaded as an ArcMap shapefile for easy integration into the project.

5.0 Processing Remote Sensing Data

5.1 DEM Processing

Previous to this study, the best available DEM of the area of interest was the DEM provided by the USGS' NED. The NED combines the best publicly available topographic data set for every region of the United States into one data layer and makes this layer available to the public. The NED DEM data set for the area of interest was derived by digitizing topographic maps from the 1960s time frame. The data was digitized to 60 meter resolution. Due to the outdated and coarse nature of the topographic maps used for DEM production, the NED DEM of the northern foothills of the Alaska Range are strongly error prone (especially in regions of high relief) and show a substantial lack of detail. This causes non-geophysical effects such as steams that flow uphill and renders this DEM largely useless for detailed geomorphic analysis. Figure 5.1 shows the NED DEM for the area of interest in a shaded relief representation. Due to the low quality of the NED DEM, the generation of an up-to-date DEM of high quality was necessary to facilitate geomorphic studies of the northern foothills. The following sections introduce remote sensing data processing that was performed to derive improved DEM information from remote sensing data.

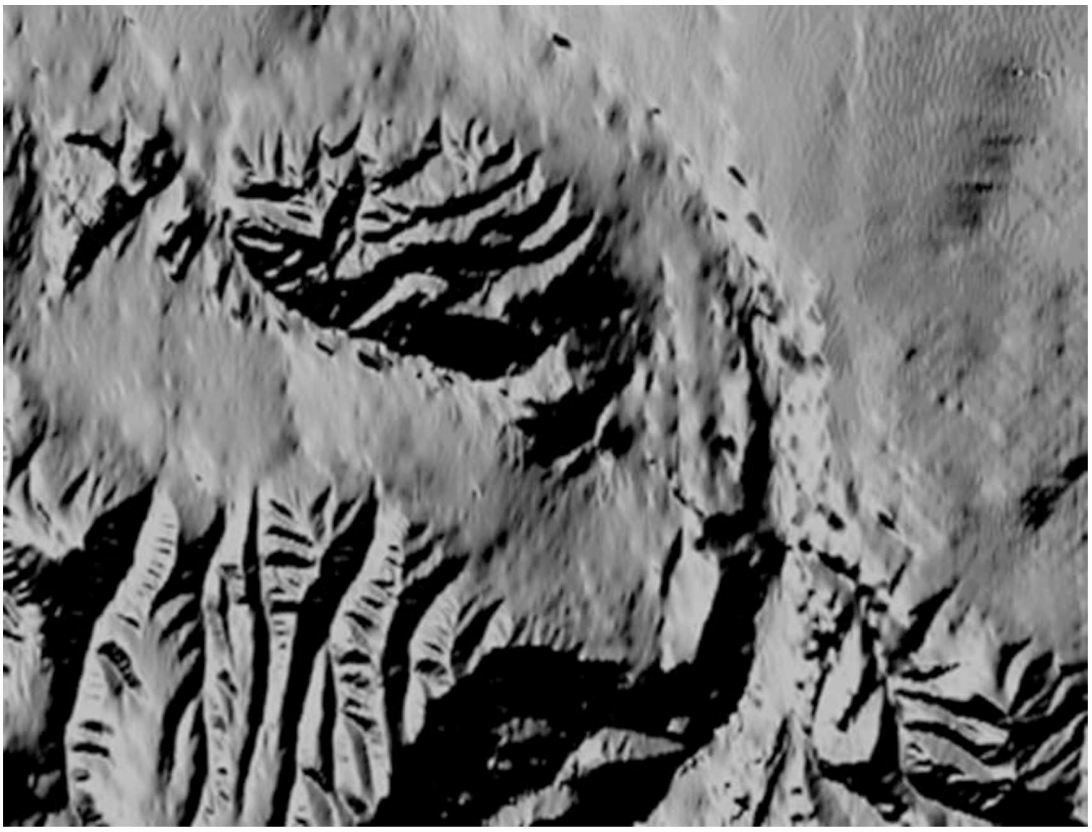

Figure 5.1 Hillshade of NED DEM. The NED DEM was interpolated from topographic maps and has a spatial resolution of 60 meters. Note that you can see the topography but not in great detail. Stepping of the DEM can be seen on the right edge of this DEM.

5.1.1 PRISM-based DEM Processing

The PRISM data was processed and mosaicked using the software package DOGS-AP, designed by JAXA specifically for PRISM data stereo processing. DOGS-AP uses PRISM image triplets acquired in forward-looking, nadir, and aft-looking geometries to calculate DEMs using stereo-photogrammetric techniques and produces DEMs with a 2.5 meter spatial resolution and a vertical accuracy in the order of about 5 meters (McAlpin and Meyer, 2012). For more information on the PRISM stereo-processing

procedures and on the specifics of the DOGS-AP software please refer to Takaku and Tadono (2009). The PRISM-derived DEM is affected by atmospheric artifacts (clouds and haze) that need to be masked. Also, due to the optical wavelengths of the data, the DEM is tracing the tops of vegetation in the area of interest, which can create significant vertical errors. To reduce noise in the produced DEM and to make the file size more manageable, the DEM was resampled to a 15 meter spacing. Despite the localized atmospheric influences, and despite of the influence of vegetation, the resulting 15 meter DEM (Figure 5.2) is a significant improvement over the 60 meter NED data. When compared to the NED DEM in Figure 5.1, Figure 5.2 specifically indicates the improved spatial detail and the reduction of artifacts in the topographic product.

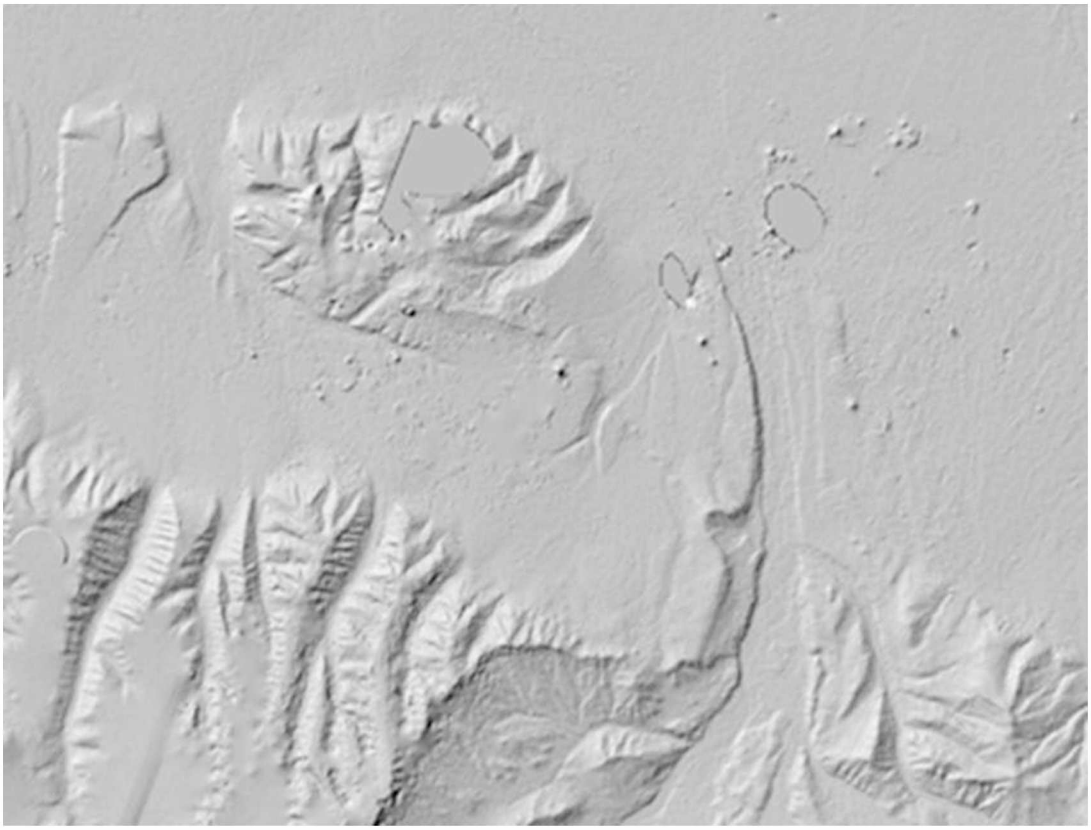

Figure 5.2 Hillshade of PRISM DSM. Hillshade created from the PRISM data that was processed by ASF to 15 meters. There is a great improvement over the NED DEM. River valleys and topography can be distinguished from the lowlands and there is no stepping of the data. In this area there are holes due to masking of clouds, some blunders from unmasked clouds and a processing error on the left edge of the image.

5.1.2 InSAR DEM Mosaicking

Towards the end of the thesis work, a new DEM data set became available that exceeded the PRISM DEM in vertical accuracy and spatial resolution. This new DEM was acquired in the framework of Alaska's Statewide Digital Mapping Initiative (SDMI) from an airborne platform using InSAR techniques. In InSAR, two SAR acquisitions from similar vantage points are co-registered and pixel-by-pixel phase differences are

calculated. This phase difference image (the so-called interferogram) is sensitive to surface topography and can be used to derive DEM information with high vertical resolution. InSAR processing of this data set was performed by FUGRO, Inc., a commercial entity that was also responsible for conducting the data acquisition. The processed InSAR DEM was provided to this research by the Geographic Information Network of Alaska (GINA), which is hosting the data acquired through the SDMI. The InSAR DEM has a resolution of 5 meters and its vertical accuracy is reported to be 2.5 – 6 meters. For more information on topographic mapping from InSAR data please refer to Hanssen (2001) and Meyer and Sandwell (2012). The SDMI elevation data has no atmospheric affects and is a true representation of the bare Earth due to the InSAR processing techniques. X-band and P-band SAR data were combined to guarantee vegetation penetration. At a resolution of 5 meters this is the best data available in the area and was hence used for further processing. As with the PRISM DSM the mosaicked 5 meter SDMI DEM is too large a file to be integrated with some of the programs needed for the project. Therefore, the data was resampled to a 10 meter resolution, resulting in 2.5GB of data. Figure 5.3 shows the InSAR DEM and indicates the high resolution and high quality of the data.

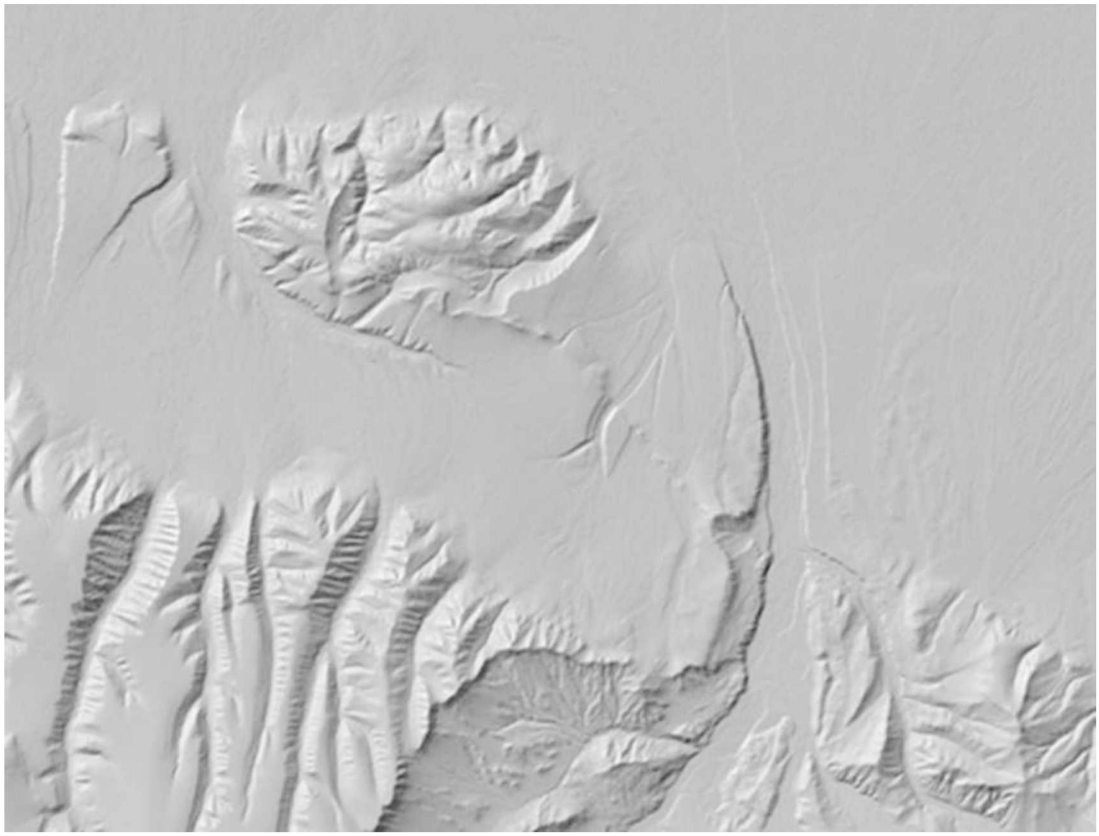

Figure 5.3 Hillshade Mosaicked DEM from SDMI data. This hillshade was created from the mosaicked SDMI data. Resolution is 10 meters and there are no atmospheric effects, the topography cleanly stands out with no blunders or seams between frames.

5.2 Fully Polarimetric SAR Data Processing

Fully-polarimetric L-band SAR data was the main data source for mapping surficial geology in the area of interest. The main goal of SAR data processing was to identify Nenana Gravel-type surfaces, as these surfaces are directly linked to neotectonic activity in the area. The processing steps presented in this section describe a data preparation procedure that was applied to fully-polarimetric SAR data. At the end of this data

preparation procedure, the radar remote sensing data is ready for geologic analysis using image classification procedures. The geologic analysis is presented in Section 5.3.

As previously stated Polarimetric SAR data was determined to be the best remote sensing data available for the classification and extraction of the extent of the preserved Nenana Gravel within the area of interest. The decision to use polarimetric SAR data was made based on its apparent stability over time and season and its sensitivity to surface structure, which is indicative of the underlying geology. As will be shown later, the polarimetric data was of sufficient quality to extract several geologic surface types using image classification algorithms. Several processing steps are required before SAR data from multiple observation times and geometries can be mosaicked into one large-coverage data layer. The processing procedure is shown in Figure 5.4, and the individual processing steps are explained in the following paragraphs.

The first step after ordering the data is to perform polarimetric processing routines that decompose the polarimetric information that is stored in the SAR data into a set of linearly independent scattering mechanisms (see Figure 3.8 for a pictographic illustration of these scattering mechanisms).

Coherence Matrix (T3 Matrix) creation: Natural surfaces such as the forests, bare surfaces, tundra, and other lightly vegetated regions in our area of interest are acting as so-called distributed scatterers when imaged by a SAR system. For distributed scatterers, the radar response is not stationary, i.e., radar brightness, phase, and

polarization are dynamically changing in space and time. To describe the scattering behavior of such target types, second-order moment descriptors need to be calculated that describe the average scattering characteristics of a surface. In monostatic image acquisition situations (transmitter and receiver are in the same location), the average scattering properties of a surface can be captured by calculating the three-dimensional polarimetric coherency matrix T3:

$$T_3 = \frac{1}{2}\begin{bmatrix} \langle|S_{HH}+S_{VV}|^2\rangle & \langle(S_{HH}+S_{VV})(S_{HH}-S_{VV})^*\rangle & 2\langle(S_{HH}+S_{VV})S_{HV}^*\rangle \\ \langle(S_{HH}-S_{VV})(S_{HH}+S_{VV})^*\rangle & \langle|S_{HH}-S_{VV}|^2\rangle & 2\langle(S_{HH}-S_{VV})S_{HV}^*\rangle \\ 2\langle S_{HV}(S_{HH}+S_{VV})^*\rangle & 2\langle S_{HV}(S_{HH}-S_{VV})^*\rangle & 4\langle|S_{HV}|^2\rangle \end{bmatrix}$$

With the measured scattering responses S_{HH}, S_{VV}, and S_{HV}, $\langle\blacksquare\rangle$ indicating spatial averages, and $\blacksquare^*$ representing the complex conjugate of $\blacksquare$. Based on the T_3 matrix, the original polarimetric SAR observations can be decomposed into a set of basic scattering principles. More information on Polarimetric decomposition can be found in Lee and Pottier (2009).

Terrain correction, geocoding, polarimetric decomposition, and GeoTIFF creation: Once the T_3 matrix is created it can then be terrain corrected and geocoded to a map projection. Following that, the coherency matrix is sent though a polarimetric decomposition model; the model chosen for this project was the Yamaguchi four

component decomposition (Yamaguchi et al., 2005). This model breaks up the data into four scattering components representing double bounce, volume scattering, helix scattering, and single bounce or surface scattering (Yamaguchi et al., 2005). Although there are 4 components of this decomposition, the helix scattering component is discarded before creating the final RGB, resulting in a color image representing the scattering power related to double bounce (red), volume scattering (green), and single bounce (blue). The helical component is a property of the signal interacting with urban structures, which in this study area are very few, and therefore can be removed without skewing the data in the study area. Once the data is decomposed it is then converted into a GeoTIFF for mosaicking and classification.

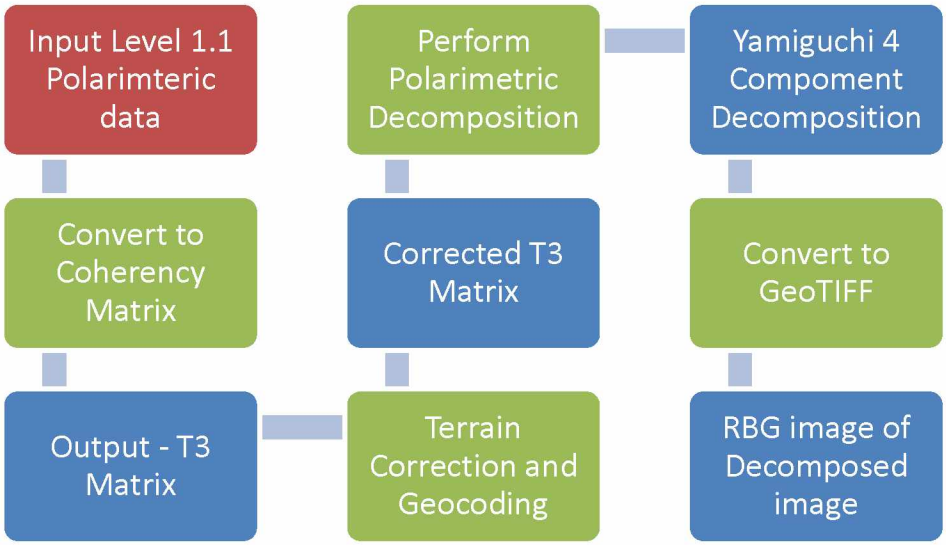

Figure 5.4 Polarimetric Processing Flow. Processing flow to convert data from amplitude data into a decomposed RGB GeoTIFF for use in geologic classification. Red is original input data, green is the processing steps, and blue are outputs.

Image mosaicking: Once the data had been converted into GeoTIFF, statistical analyses were performed to identify images that show statistically identical scattering information and can therefore be seamlessly mosaicked. First, a set of test plots were identified for which radiometric properties were compared. The plots were selected to coincide with known areas of Nenana gravel, as this surface type was of most interest in this study. Second, box plots were created representing statistics of the surface scattering (blue) component of the geocoded RGB images. A total of 31 scenes were analyzed in this fashion, covering the entire area of interest over a time span of 3 years. Scene names and dates of acquisition can be found in Table 5.1. In this table, images are sorted according to the day of the year of acquisition to be able to easily analyze seasonal dependencies in scattering power.

Table 5.1- List of SAR data for Mosaic. Table includes an identifying number for box plots and comparison of mean plots, scene name, date of acquisition, winter scene designation and the data included in the final mosaic.

Identifier for Plots	Scene Name	Date	Winter Scenes	Included in Final Mosaic
1	ALPSRP059551280, ALPSRP059551290	3/8/2007	X	
2	ALPSRP166911280, ALPSRP166911290	3/13/2009	X	X
3	ALPSRP060281280, ALPSRP060281290	3/13/2007	X	
4	ALPSRP167641280, ALPSRP167641290	3/18/2009	X	X
5	ALPSRP114981280, ALPSRP114981290	3/22/2008	X	
6	ALPSRP168661280, ALPSRP168661290	3/25/2009	X	X
7	ALPSRP062031280, ALPSRP062031290	3/25/2007	X	
8	ALPSRP115711280, ALPSRP115711290	3/27/2008	X	
9	ALPSRP169391280, ALPSRP169391290	3/30/2009	X	X
10	ALPSRP117461280, ALPSRP117461290	4/8/2008	X	X
11	ALPSRP064511280, ALPSRP064511290	4/11/2007		
12	ALPSRP171141280, ALPSRP171141290	4/11/2009		
13	ALPSRP224821280, ALPSRP224821290	4/14/2010		
14	ALPSRP171871280, ALPSRP171871290	4/16/2009		
15	ALPSRP066991280, ALPSRP066991290	4/28/2007		
16	ALPSRP068011280, ALPSRP068011290	5/5/2007		
17	ALPSRP121691280, ALPSRP121691290	5/7/2008		
18	ALPSRP175371280, ALPSRP175371290	5/10/2009		
19	ALPSRP122421280, ALPSRP122421290	5/12/2008		
20	ALPSRP070491280, ALPSRP070491290	5/22/2007		
21	ALPSRP124901280, ALPSRP124901290	5/29/2008		
22	ALPSRP126651280, ALPSRP126651290	6/10/2008		
23	ALPSRP128401280, ALPSRP128401290	6/22/2008		
24	ALPSRP184561280, ALPSRP184561290	7/12/2009		
25	ALPSRP238241280, ALPSRP238241290	7/15/2010		
26	ALPSRP093101280, ALPSRP093101290	10/24/2007		
27	ALPSRP201191280, ALPSRP201191290	11/3/2009	X	
28	ALPSRP148531280, ALPSRP148531290	11/7/2008	X	
29	ALPSRP202211280, ALPSRP202211290	11/10/2009	X	
30	ALPSRP202941280, ALPSRP202941290	11/15/2009	X	
31	ALPSRP204691280, ALPSRP204691290	11/27/2009	X	

The box plots resulting from this analysis are shown in Figure 5.5. From this figure, three main conclusions can be draw: (1) a clear seasonal dependence of scattering behavior can be identified with winter scenes showing very consistent lower amplitude scattering behavior and summer scenes exhibiting more variable, higher amplitude scattering properties; (2) the scattering behavior is very consistent throughout the four years across which the data is spread; (3) from the shape of the box plots (mean value near the middle of the boxes) it can be seen that the image data has near Gaussian properties. This is due to the averaging process that was applied when calculating the coherency matrix. Especially for the winter acquisitions, no dependence on the year of acquisition can be seen. Based on these results, it was concluded that winter acquisitions are more suitable for mosaicking. Therefore, summer data was discarded from further analysis. The scenes used in the final mosaic are marked with crosses in column five of Table 5.1.

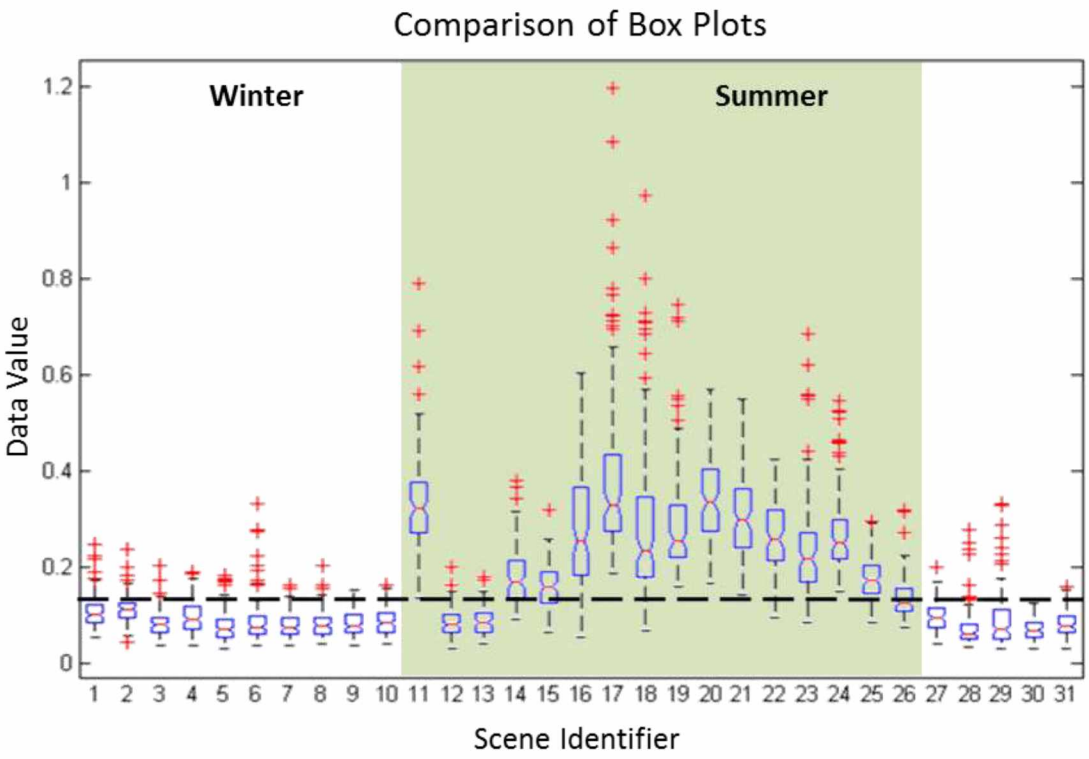

Figure 5.5 Comparison of Box Plots Over Time. Comparison of box plots over time for all of the scenes in the study area. Scene identifier coincides with Table 5.1, and the data varies significantly more over the summer months (highlighted in green) then the winter months.

To further analyze statistical differences between the selected winter scenes, an Analysis of Variance (ANOVA) was performed, testing for whether or not all winter acquisitions are statistically identical. While the ANOVA test was rejected (stating that at least one image behaves differently from the rest), the sample post-hoc, multiple comparison of means test shown in Figure 5.6 indicates that most images are statistically identical and the outliers are few.

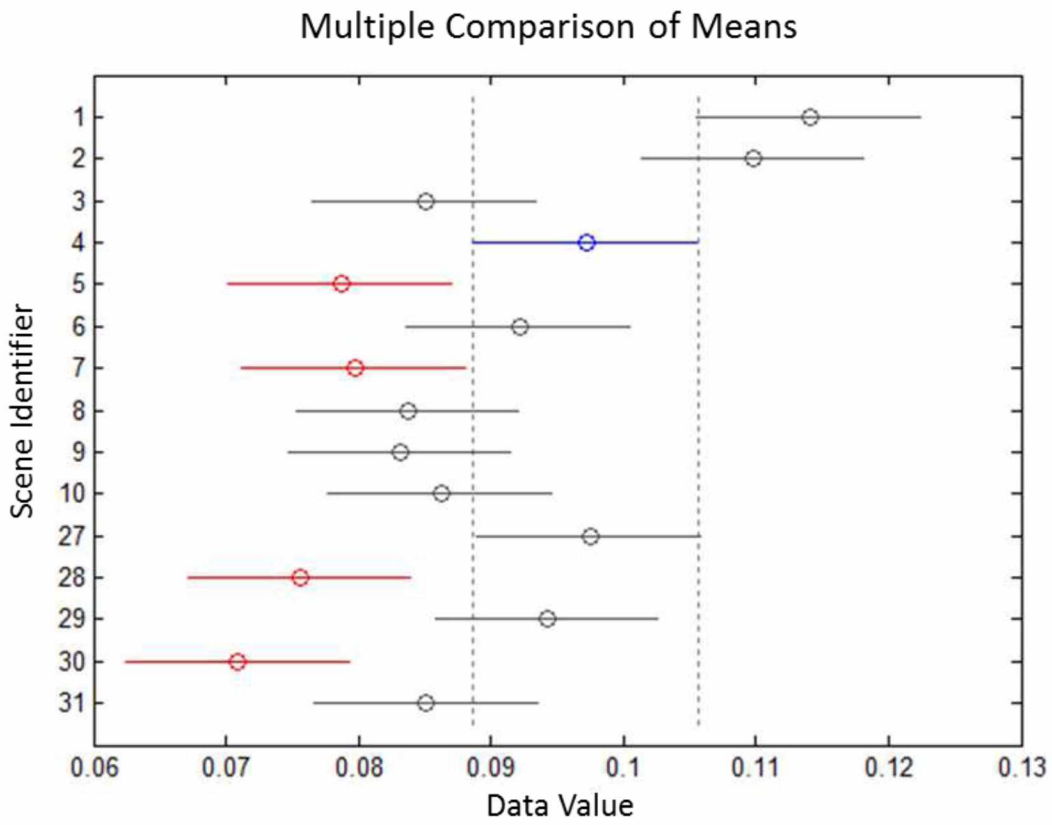

Figure 5.6 Multiple Comparison of Means Winter Plot. Multiple comparison of means compares the means of the data with the variation of the data around adjacent means. Shown here most of the winter data is significantly similar (gray) to scene four (blue), to include in a mosaic with that image. Images not significantly similar to scene four (blue) were excluded (red).

In Figure 5.6, the scene marked in blue is tested against all other winter scenes. Images marked in gray are statistically identical while scenes marked in red have statistically significant scattering differences. Based on post-hoc tests, a final set of winter scenes to be used in the final mosaic were selected (see Table 5.1, column 5). Unfortunately, due to this selection approach, a narrow sub-region of the northern foothills is missing in the final image mosaic.

Final image mosaicking was based on the ENVI software package and used the following processing steps, depicted in figure 5.7. First the GeoTIFFs were entered into the program. Second, the "Mosaicking by Georeference" tool was used and data was imported. Once the selected data was in the tool the background gray value was set to be ignored in image mosaicking and mosaicking was started.

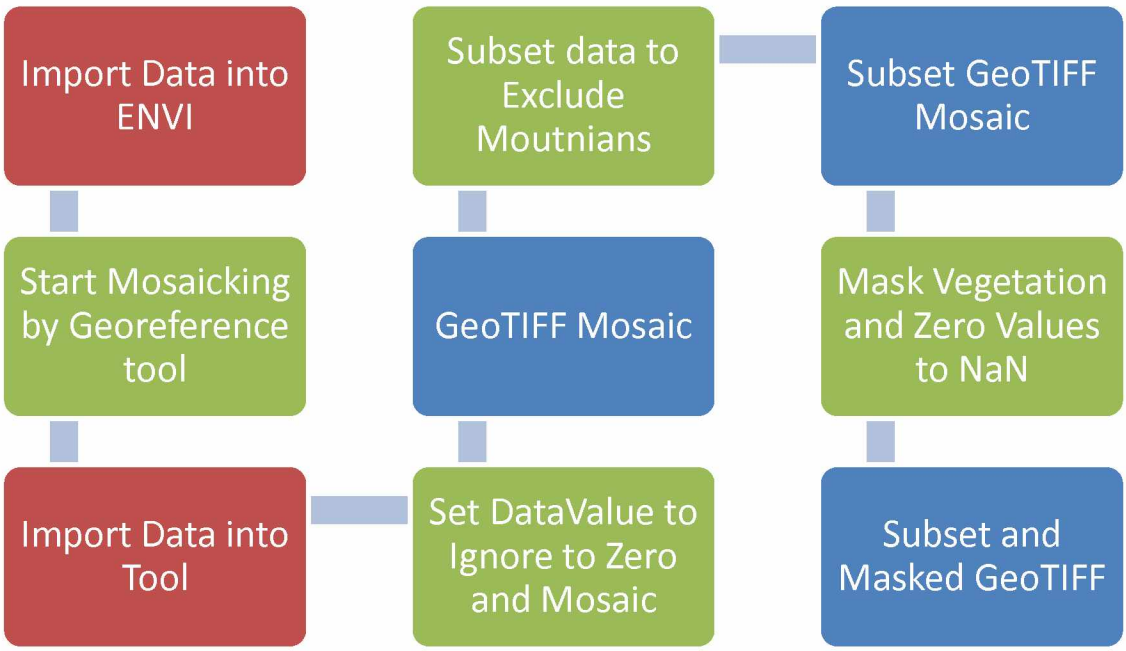

Figure 5.7 Mosaic Processing Flow. Processing flow to mosaic data into a single GeoTIFF for use in geologic classification. Red are the tools, green is the processing steps, and blue are outputs.

As a consequence of the geometric errors in the SAR data related to the steep slopes of the mountains in the southern part of the mosaic, I subset the GeoTIFF to exclude that area. The final image mosaic product is shown in Figure 5.8.

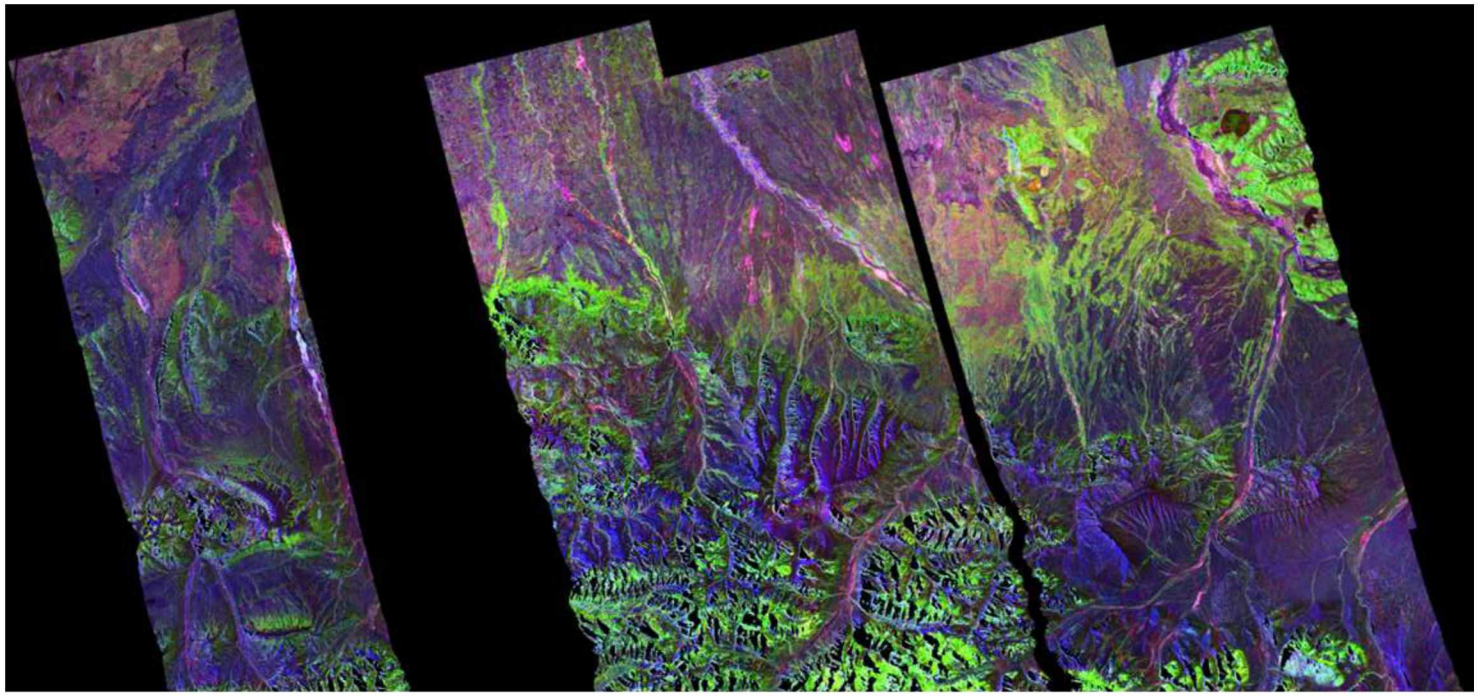

Figure 5.8. Final Polarimetric SAR Mosaic. Final output of the Polarimtric SAR Yamiguchi four component decomposition with background data value set to NaN.

Due to the possibility of vegetation having an effect on the SAR backscatter and possibly skewing the classification, a vegetation mask was applied to the mosaic. The mask was derived from the NLCD land cover dataset and was used to mask out tall trees, woody wetlands, and water. The mask left areas covered by small trees, brush, tundra, grass, bare rock and fire scars in the final image and therefore available to be classified. The masked product that was used in the classification is shown in Figure 5.9. All of the areas in the final image that are seen as black (Figure 5.9) have a “not a number” or NaN value and will not be included in the final classification.

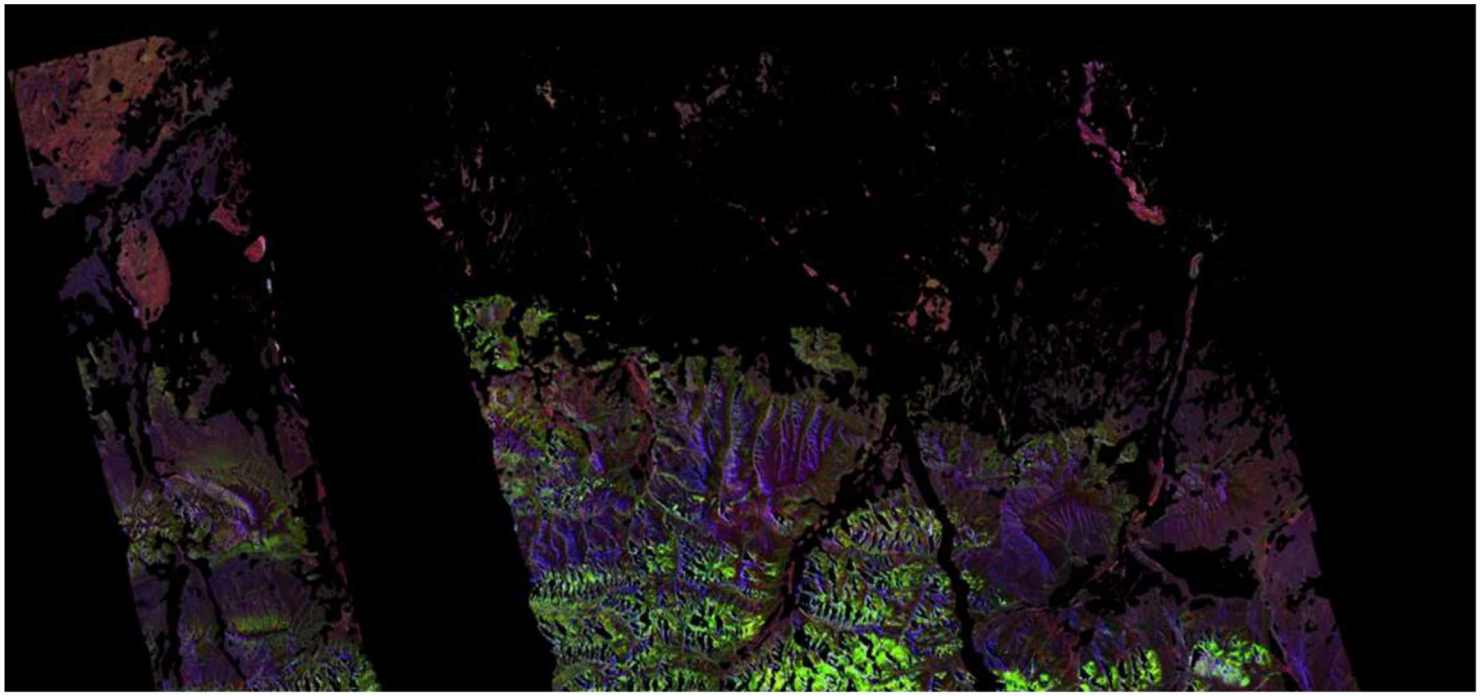

Figure 5.9. Masked Polarimetric SAR Mosaic. Polarimetric SAR Yamiguchi four component decomposition with applied vegetation mask. All areas in black have been excluded from the final classification.

5.3 Classification of Mosaicked SAR data

Since the SAR data has been successfully transformed into a decomposed mosaicked image, it is now possible to perform a classification across the entire area of interest. The classification will be primarily used to identify the preserved depositional surface of the Nenana Gravel. The classification processing flow can be found in Figure 5.10. The classification results representing preserved Nenana Gravel can then be overlaid onto a current DEM for future studies to analyze the shape and determine the attitude of the thrust faults causing the uplift. There are two main methods for classifying data, supervised and unsupervised classification, which were applied in this study, and the goal of both is to put every pixel of the image into a distinct group or class.

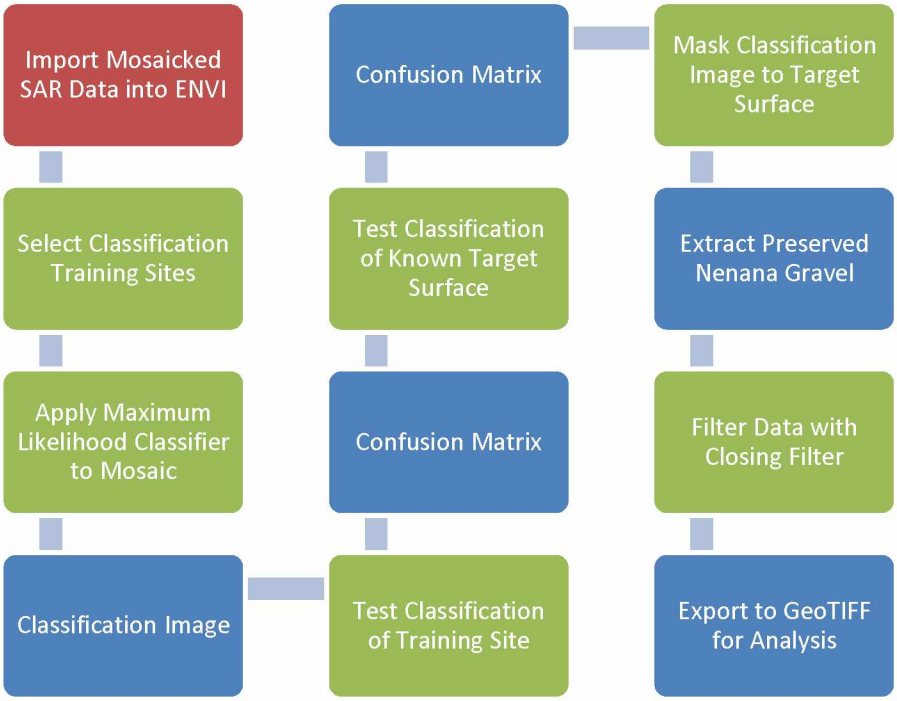

Figure 5.10 Surface Extraction Processing Flow. Import data is in red, processes are in green and outputs are in blue.

5.3.1 Unsupervised Classification

The unsupervised classification classifies the data based on natural groupings of pixels in the three-dimensional gray value space. Without the need for external information, the data is automatically broken up into a (user defined) number of clusters based on the natural clustering of the image data. After cluster centers are identified, all pixels are assigned to the closest cluster using some form of a distance metric. Unsupervised classifiers provide a largely unbiased means to group image data. It also is a good tool for exploring the natural clustering of the observations. Two common unsupervised classification algorithms are (1) the **K-means** and (2) the **Iterative Self-Organizing Data Analysis Techniques A**^{2} or **Isodata** techniques. For the K-means classification the user defines the number of clusters of data. The classifier then determines the center of the cluster and each pixel is then assigned to a cluster based on the distance to the closest mean. After all of the pixels have been classified, the means are recalculated and each pixel is then assigned to a cluster based on the distance to the closest mean (again); this continues until there is no significant change in the mean values. The Isodata techniques builds on the K-means but uses the statistics of the cluster to merge, split, delete or create new clusters. This continues until there is no significant change in the cluster statistics or a pre-determined number of iterations is reached. Both a K-means and an Isodata classification were conducted on a subset of the mosaic in the Japan Hills area to determine if there was separability between natural clusters with the SAR data, and in each case a definite separability between classes was observed (Figure 5.11). Knowing

that there is separability, a supervised classification with trained data should be able to refine the classes.

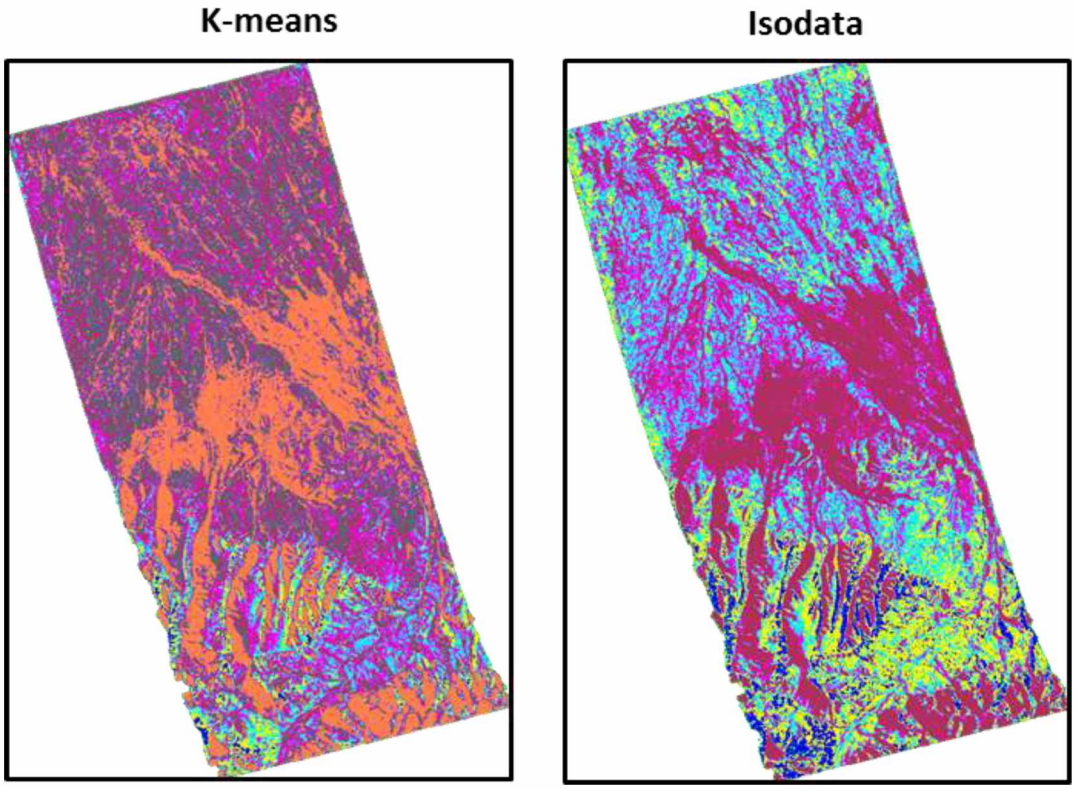

Figure 5.11 Unsupervised Classifications. Unsupervised classification of a subset of the study area that shows there is separation between classes. Refinement of these classes can be achieved with a supervised classification.

5.3.2 Training Data

Supervised classifiers use the statistics of specific training sets to determine cluster centers and group pixels to these centers using a distance measurement. A training set of pixels is a collection of pixels that represents all surface classes that are of interest in a certain application. In the case at hand, I am looking at surface geology and need to

choose pixels that represent specific stratigraphic units in the area. The training set needs to represent each unit while avoiding pixels of a mixed surface type, because the statistics of the training pixels is what the classifier is based on. For most of the supervised training algorithms the more pixels there are in a training set the more accurate the classifier is. This statement is true for all applied supervised classifiers with the exception of the Support Vector Machine classifier. The training set should also be dispersed spatially, to ensure representation of the variation of the unit. The classes defined for the project are (i) the preserved depositional surface of the Nenana Gravel (target surface), (ii) the eroded Nenana Gravel, (iii) the Usibelli Group and schist cores, (iv) Spruce Creek sequence, and (v) fire scars. I separated the Nenana Gravel into two groups so that the preserved surface would be distinguishable and extractable for further use. The Usibelli Group and the schists were very difficult to separate in the data and since they were not the target surface I joined the two into a single class. The Spruce Creek sequence was very distinctive in the southern portion of the study and was therefore added as an additional class. Finally there is a fire scar in the Tanana Basin that was not masked out by the vegetation mask and was very distinct in the SAR data, so a class was also created for that.

5.3.3 Supervised Classifications

Supervised classifiers also group the pixels into classes, but unlike the unsupervised classifiers that use the statistics based on natural groupings of pixels, they rely on statistics of predefined training pixels. The following four very common supervised classifiers were considered and tested for performance: (1) The **Minimum Distance** classifier assume a Gaussian distribution of the data and calculates the mean value of the samples in each training set. Then unknown pixels are assigned to a class depending on the Euclidean distance of its gray value to the mean value of the surrounding classes. Pixels are assigned to the nearest class. This classifier has the advantage that is very fast and computationally efficient. However, its performance is limited by the fact that it does not take into consideration the variance of the class data. (2) The **Parallelepiped** classifier determines the minimum and maximum values of a class (from the training data) and uses these to determine the class space. Class thresholds (boundaries) are determined using the standard deviations of the class means. In this classification, pixels that fall outside of the determined class boundaries are not classified. This is also a very fast classifier, but it does not take into account the variance of the data, does not classify all image pixels, and is known to be not very accurate. (3) The **Maximum Likelihood** classifier assumes a Gaussian distribution of the data like the Minimum Distance classifier, but is based on probability instead of the mean values. It calculates an *a priori* probability density function for all classes based on the training data and uses equi-probability contours to determine which class a pixel may belong to. It then uses a

probability density function to assign a pixel to the class with the highest probability and utilizes distance, variance and co-variance. Finally, (4) the **Support Vector Machine** is a linear classifier that separates two classes by defining a best-separating linear hyper-plane between them. This ideal hyper-plane is one with the maximum margin between it and the nearest data points. This classifier is ideal if the quality of the training data is high and the number of training samples is low. If, however, the quality of the training data is limited, like it is the case in this study (there is some underlying uncertainty in the training sets), the performance of support vector machines will go down. While there are rules that can be implemented to overcome noise-related classification issues, no rule could be found that would lead to satisfactory classification results for this data. Given the above considerations, the Maximum Likelihood classifier was chosen as the most appropriate classification method for this study. For more information regarding supervised classifiers see Lillesand et al. (2008).

5.3.4 Classification Process and Data Extraction

I chose to use the Maximum Likelihood classifier due to it utilizing the variance and covariance to determine probability class determination. As the SAR data was averaged over a 3x3 window during the calculation of the coherency matrix, the image information is of near Gaussian nature, allowing for the application of a maximum likelihood classification scheme.

The first step of the classification procedure is to define training sites (see Section 5.3.2 Training Data) for every surface class, which I did using the geologic maps created by Clyde Wahrhaftig (1970a-h). These maps provided critical outlines for determining where the training data should be collected. The only class that was not defined by the geologic maps is the fire scar class, which was derived from the outlines of past wildfires. The locations of the training sites for each relevant surface class are summarized in Figure 5.12.

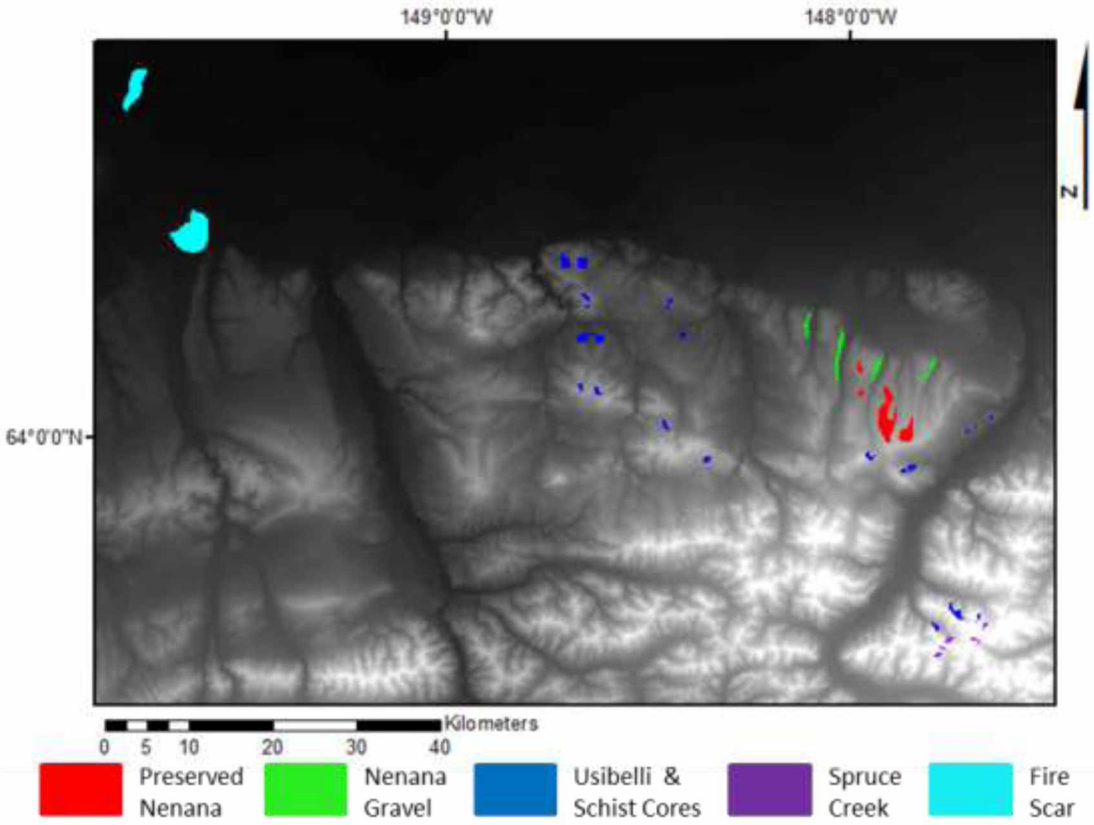

Figure 5.12 Training Classes Overlaid on DEM. Overlay of training set onto a DEM of the area. Training data was separated into five classes: preserved Nenana surface (red), eroded Nenana Gravel (green), Usibelli Group combined with exposed schist (blue), Spruce Creek sequence (purple) and fire scar (cyan). The five classes outline the statistics to be used in the final classification.

I then applied the Maximum Likelihood classification to the image data using the identified training data. The resulting classified image, made up of the five classes, is presented in Figure 5.13.

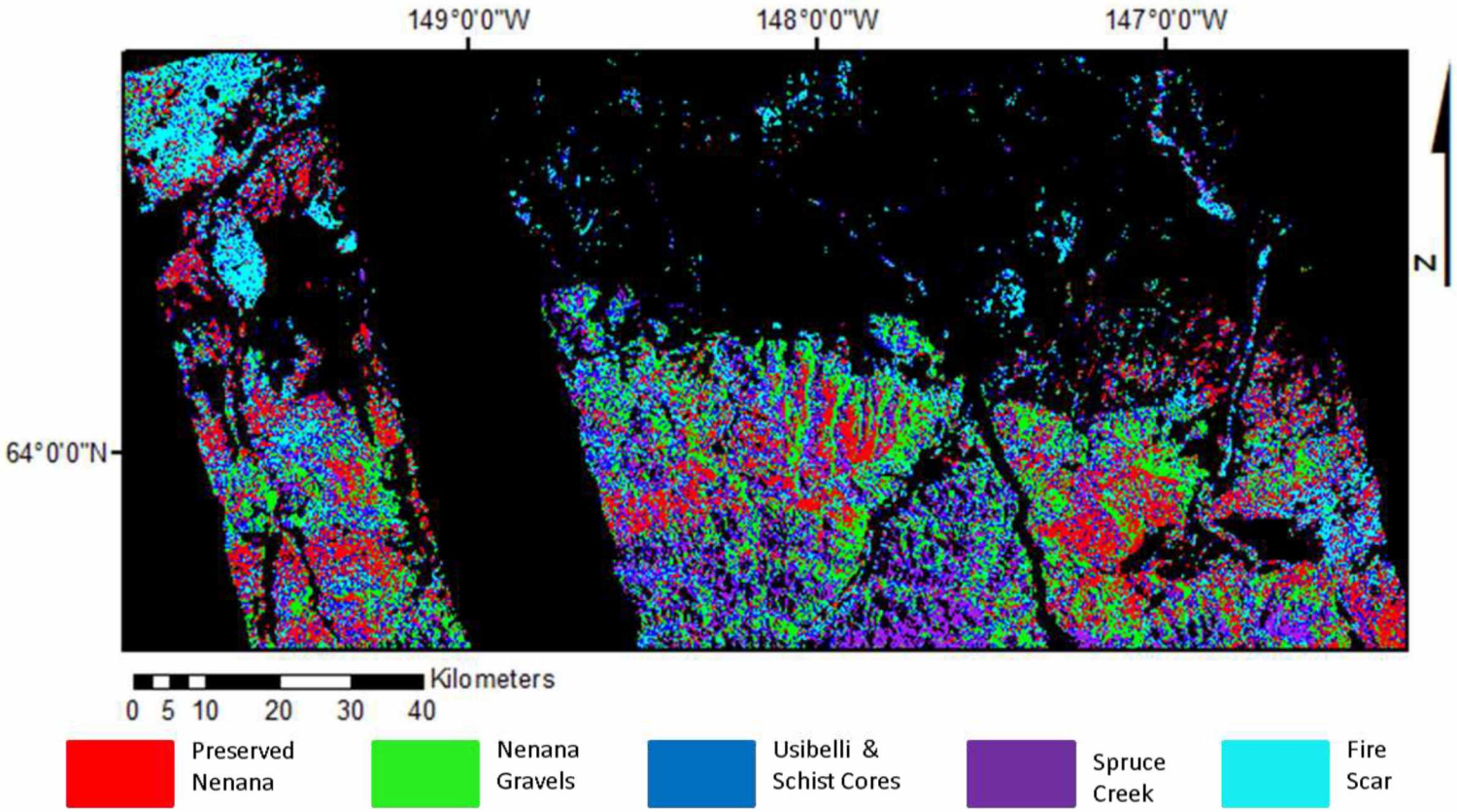

Figure 5.13 Maximum Likelihood Classification. Classification of masked polarimetric SAR data mosaic of the area. The preserved surface of the Nenana gravels (red) is the target surface for extraction, and clearly shows up in this classification.

To test the accuracy of image classification, a confusion matrix was computed. This matrix analyzes all training pixels and determines if the pixels within the training areas were classified correctly. The confusion matrix is presented in Table 5.2 and indicates that the classification had an overall accuracy of 72.81%, with individual classes having the following accuracies: Preserved Nenana Gravel – 94.92%; Eroded Nenana Gravel – 89.4%; Usibelli Group & Schist – 24.75%; Fire Scar – 84.33%; and the Spruce Creek sequence - 99.35% (Table 5.2). These results show that most classes can be separated successfully and with high quality. An exception is the "Usibelli Group & Schist" class that was difficult to discriminate from other classes given the selected training data. In particular, it should be noted that the target surface of the Preserved Nenana Gravel could be identified with high quality. To test the classification of the preserved Nenana Gravel outside of the training areas I created a second set of test sites, completed a second confusion matrix with those areas, and compared this second matrix to results within the training sites.

Table 5.2 Confusion Matrix of Training Sites. Table of how the classifier placed all the pixels with the training areas. Preserved Nenana Gravel surface and Paleozoic bedrock had the highest percent correct, while the Usibelli Group and Schist combination was difficult for the classifier to differentiate from other classes.

Class	Preserved Nenana Surface	Eroded Nenana Gravels	Usibelli Group & Schist	Fire Scar	Spruce Creek
Preserved Nenana Surface	***94.92***	1.38	18.81	3.00	0.00
Eroded Nenena Gravel	1.38	***89.40***	31.82	1.40	0.00
Usibelli Group & Schist	1.66	7.20	***24.75***	10.98	0.65
Fire Scar	2.01	1.96	21.88	***84.33***	0.00
Spruce Creek	0.02	0.06	2.74	0.29	***99.35***
Total	100	100	100	100	100

This comparison is shown in Table 5.3. Overall results of the independent test sites were highly comparable to the results based on the original training sites, indicating that the classification result can be deemed reliable. Although this classification performed well, a correlation of some of the classes with topographic features can be identified in Figure 5.13. This can be, in part, due to remaining topography-related radiometric distortions of the SAR data (Section 3.3.2 Terrain Correction), affecting sensor-facing slopes of the image. While such effects can be seen in some of the eroded valleys in the area, they did not affect the classification of the preserved Nenana Gravel due to the relative flatness of that preserved surface.

Table 5.3 Test Area vs. Training Set Confusion Matrix. Table compares the percent of pixels classified as all classes for both the training set and the independent test sites.

Class	Preserved Nenana Surface	Independent Test Sites
Preserved Nenana Surface	***94.92***	***90.67***
Eroded Nenena Gravel	1.38	4.51
Usibelli Group & Schist	1.66	4.36
Fire Scar	2.01	0.39
Spruce Creek	0.02	0.04
Total	100	100

Since the classification tested well, the preserved Nenana Gravel was extracted using the ENVI band-masking tool by assigning a value of one to the Nenana Gravel class pixels and a value of zero to all the other classes, effectively isolating the Nenana Gravel from the rest of the image. Figure 5.14 shows the resulting Preserved Nenana Gravel mask. The extracted data includes pixels that were classified as a single pixel and are not part

of a cluster. These lone pixels are scattered throughout the image, making it look noisy. To reduce this classification noise, the data was filtered using morphological filters. Specifically, a morphological opening filter was applied that removes all pixels that were not at least three pixels from a central data point, affectively constraining the data to areas of continuous target surface (see Figure 5.15 for the filtered "Preserved Nenana Gravel" mask). For more information on morphological filters see Castleman (1996).

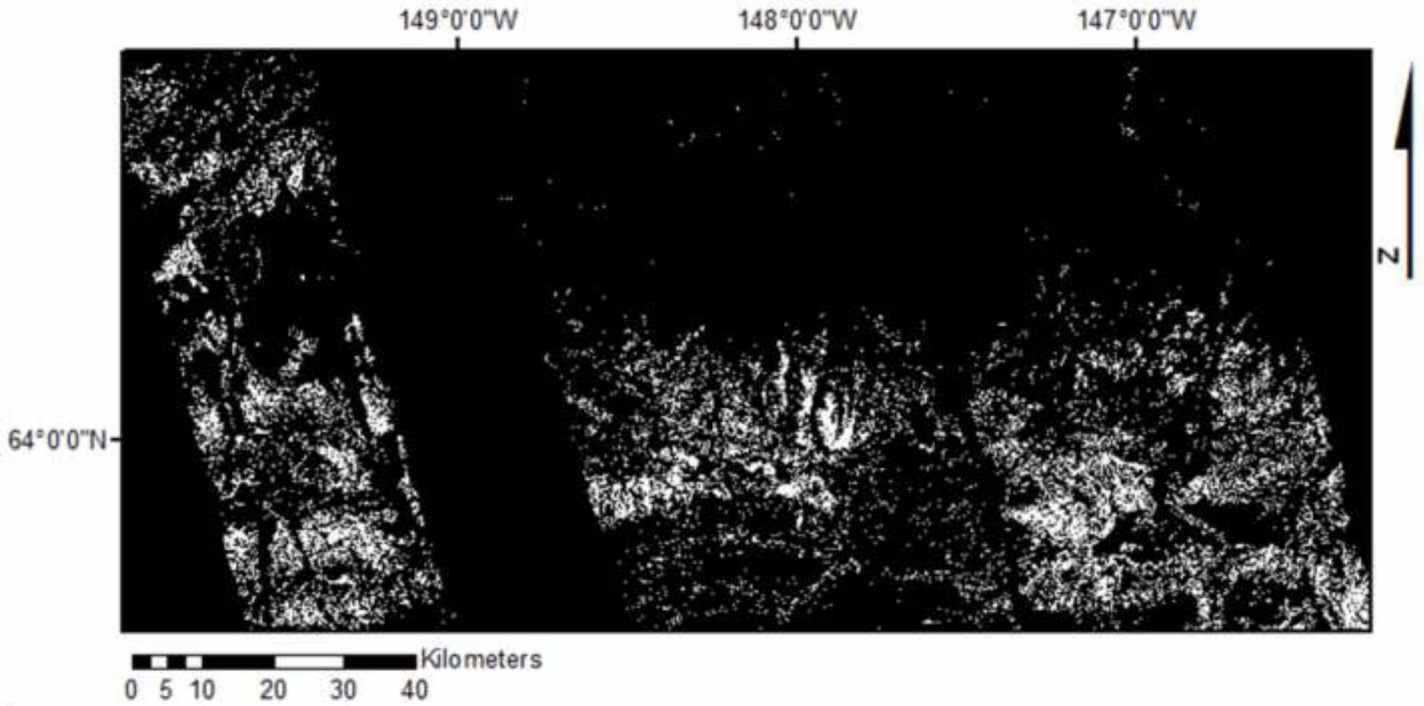

Figure 5.14 Extracted Nenana Gravel Class. White are the pixels that were classified as Preserved Nenana Gravel surface. Note there are many small groupings of pixels scattered throughout the image.

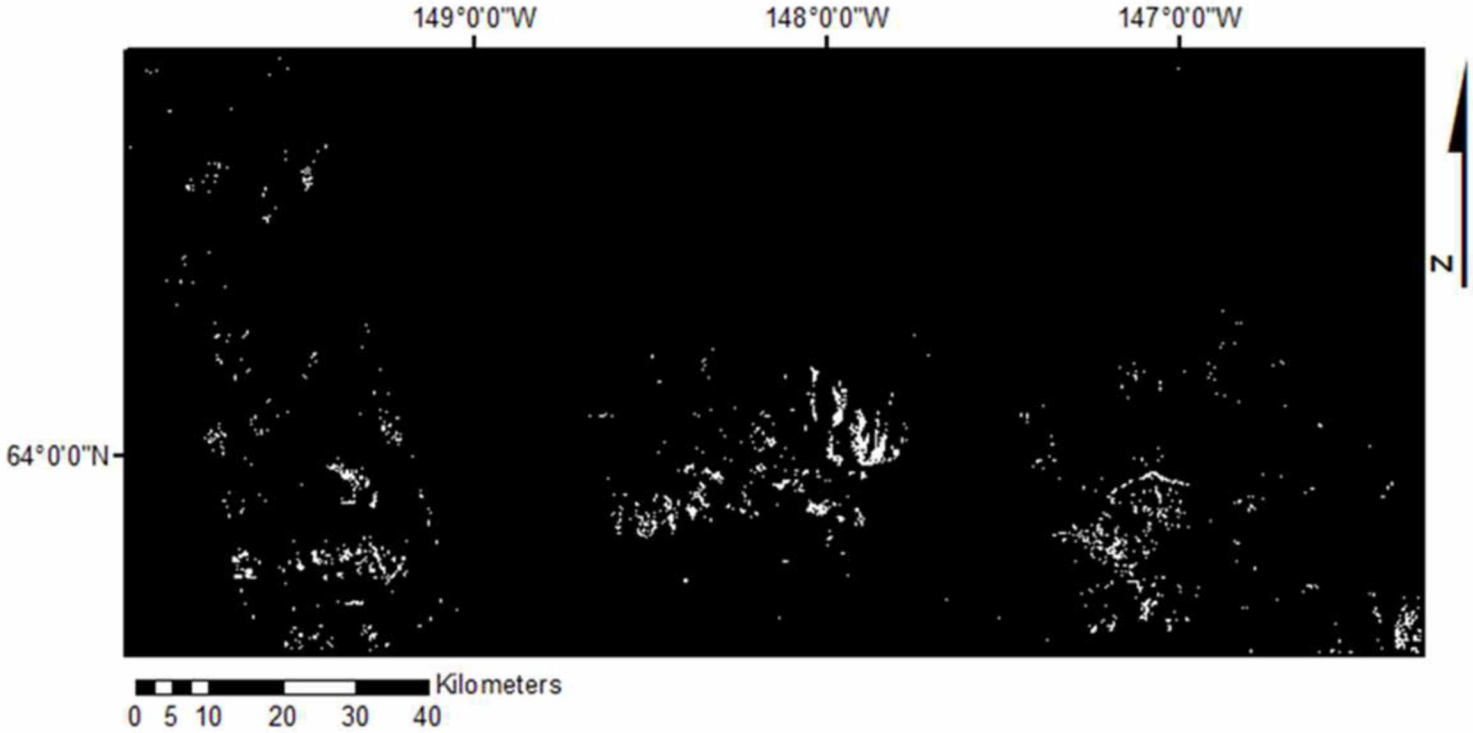

Figure 5.15. Filtered Extraction of Nenana Gravel Class. Image has been filtered with a 3x3 opening morphology filter. This has effectively reduced the number of orphan pixels and concentrated the information in the areas most likely to be the target surface.

6.0 Geologic Analysis

6.1 Preserved Nenana Gravel Surface

To help with visual interpretation, the extracted preserved surface of the Nenana Gravel (referred to as preserved surface from now on), was overlain on a hillshade image created from the 10 meter DEM. Figure 6.1 shows the extracted and filtered preserved surface (blue) and extent of the Nenana Gravel (red outlined areas) overlain on the DEM hillshade. It can be seen that most of the extracted preserved surface (blue) lies within the borders of the previously mapped Nenana Gravel. However, there are some areas where the preserved surface (blue) is not located within the borders of the mapped extent of Nenana Gravel. This could be due to similar lithologies, such as the Usibelli group and Quaternary terrace deposits having depositional surfaces similar to that of the Nenana Gravel.

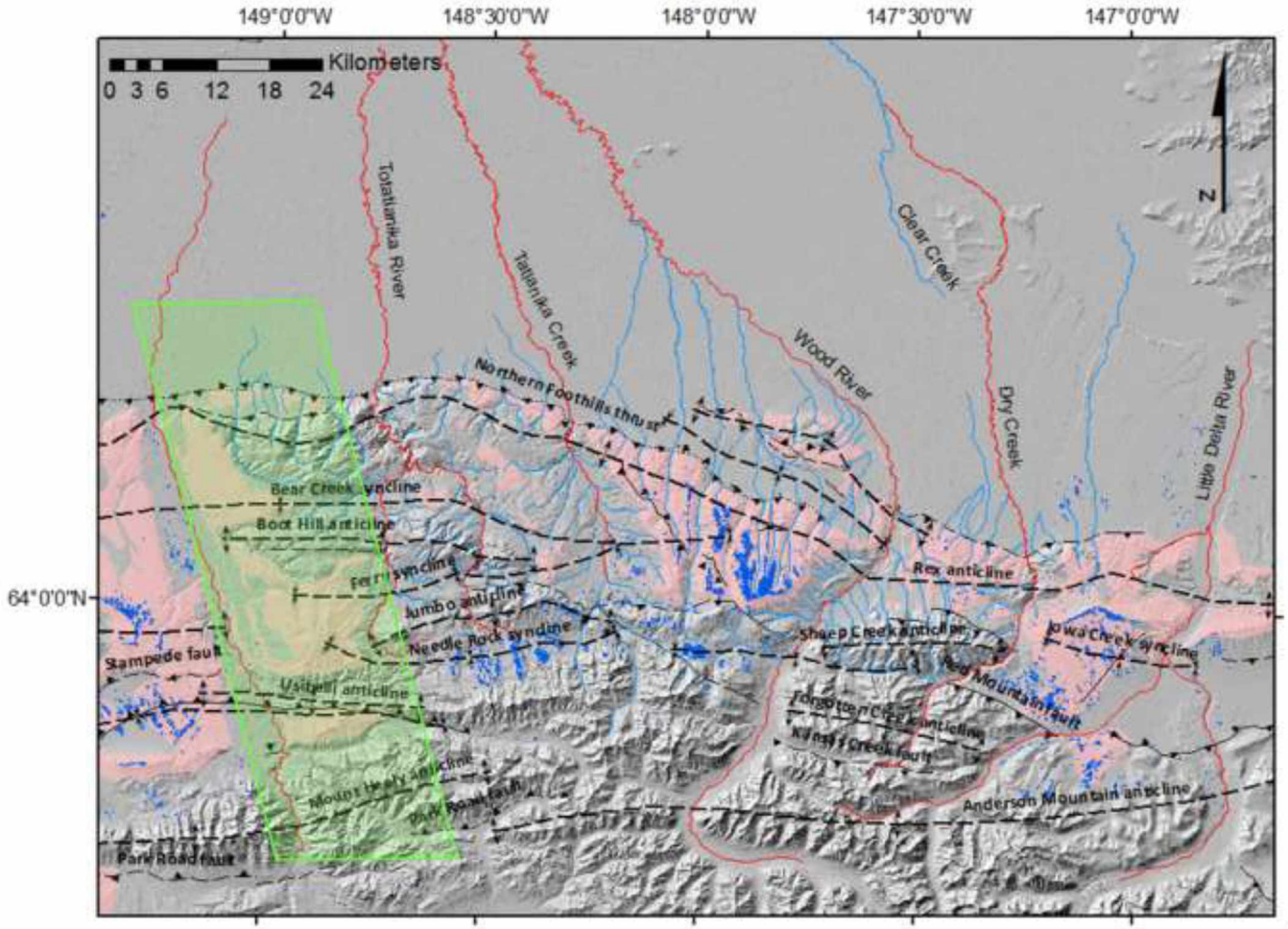

Figure 6.1 Classified Preserved Surface vs. Mapped Nenana Gravel. Mapped extent of the Nenana Gravel (red polygons) and extracted preserved surface (blue) overlain on hillshade of 10 meter InSAR derived DEM. The green box indicates the area of missing SAR data so there is no classified preserved surface data there.

The preserved surface as determined from the classification and overlain on a hillshade image derived from the 10 meter DEM is shown obliquely in Figures 6.2, 6.3, and 6.4, which are all displayed with a vertical exaggeration of 4 times. Synclines are shown as yellow hashed lines, anticlines are red hashed lines, and faults are solid green lines. This type of visualization highlights the geometry of the neotectonic deformation along the range front. Figure 6.2 clearly shows that the preserved surface has been uplifted and folded in a rounded anticline-syncline pair.

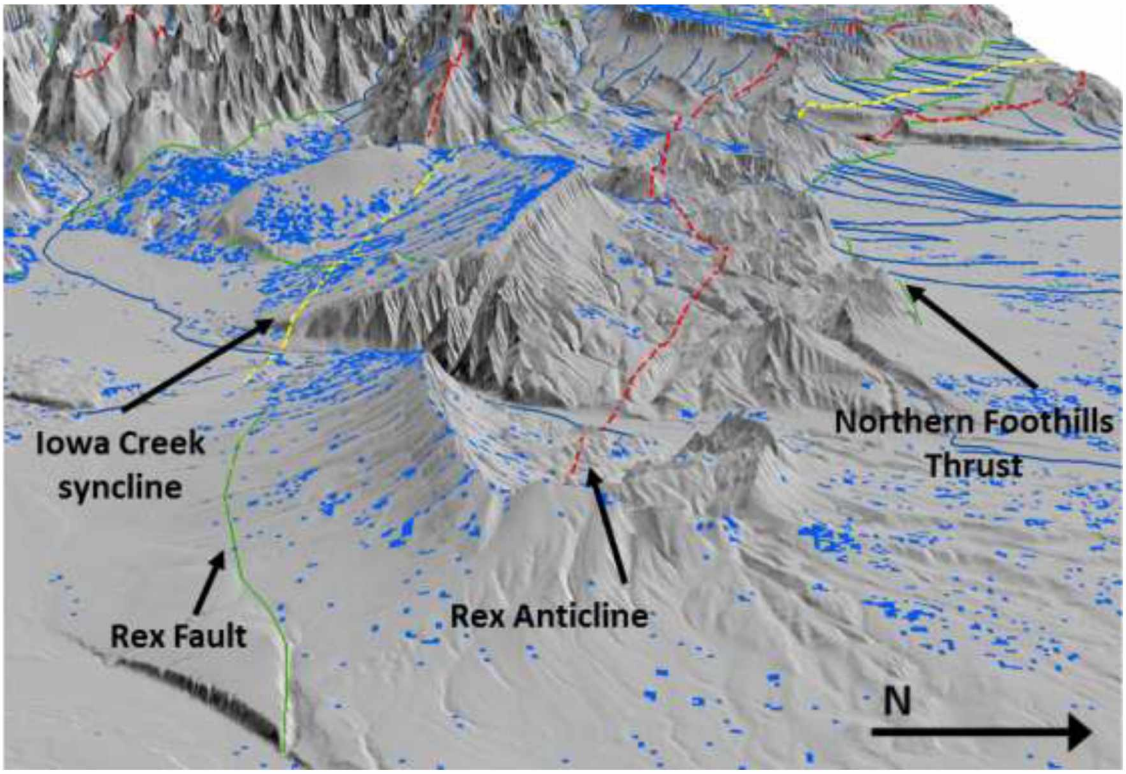

Figure 6.2 Extracted Surface Overlay, Eastern Region. Overlay of preserved surface on hillshade image draped over the DEM in the eastern part of the study area. The preserved surface (blue) has been folded during the growth of the Iowa Creek (yellow hashed line) and Rex (red hashed line) anticline-syncline pair. Faults are solid green lines.

In Figure 6.3, the surface is situated on top of the very gently north-dipping backlimb of a flat-topped monocline that is bounded to the north by the Northern Foothills thrust. The Rex "anticline" is the hinge of this monocline and, while the classification only picked up a few bits of the steep north limb, it is well defined by the topography. To the south across an erosional gap, the preserved surface clearly defines the Needle Rock syncline.

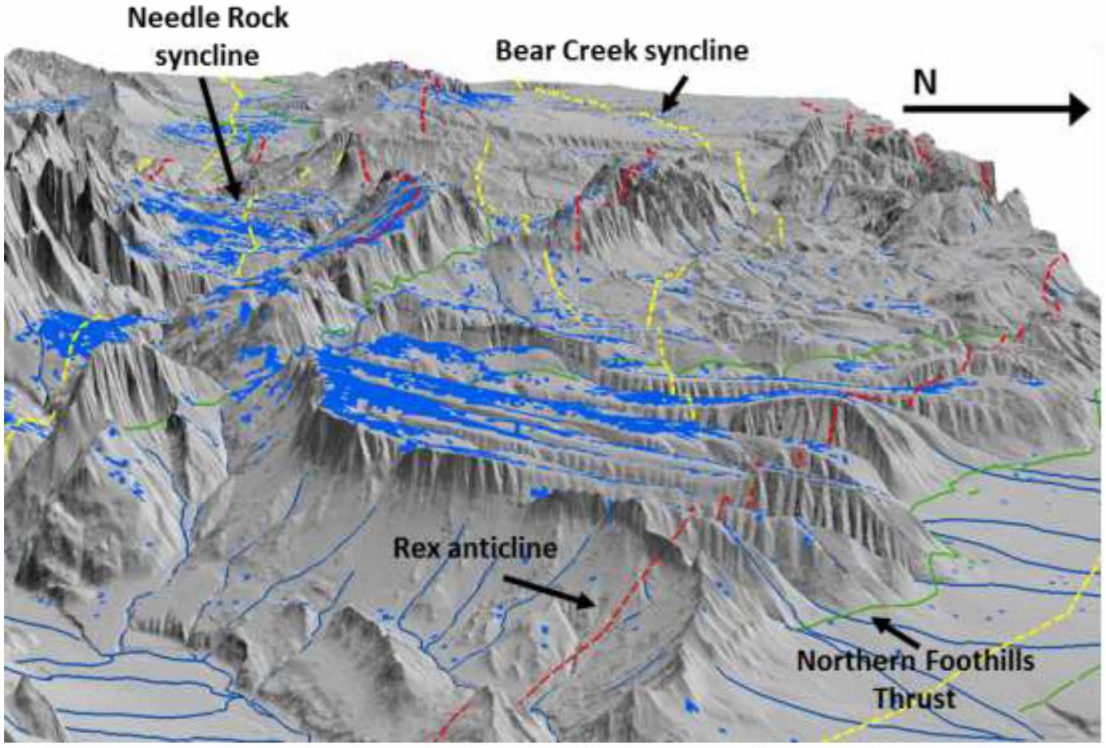

Figure 6.3 Extracted Surface Overlay, South of the Japan Hills. Distribution of the preserved surface (blue) between the Needle Rock syncline and the Rex anticline is shown here in blue. Location of the Northern Foothills thrust fault, and other area faults are shown as green lines, the synclines are yellow hashed lines and anticlines are shown as red hashed lines and labeled with arrows.

In the far west of the study area west of the Nenana River, the preserved surface is exposed over a large area from the Bear Creek syncline to the north, south over the Stampede anticline, into the Eight-Mile Lake syncline and up onto the north limb of the Mt. Healy anticline. The folding of the surface shows that the deformation happened after the deposition of the Nenana Gravel in this area (see Figure 6.4).

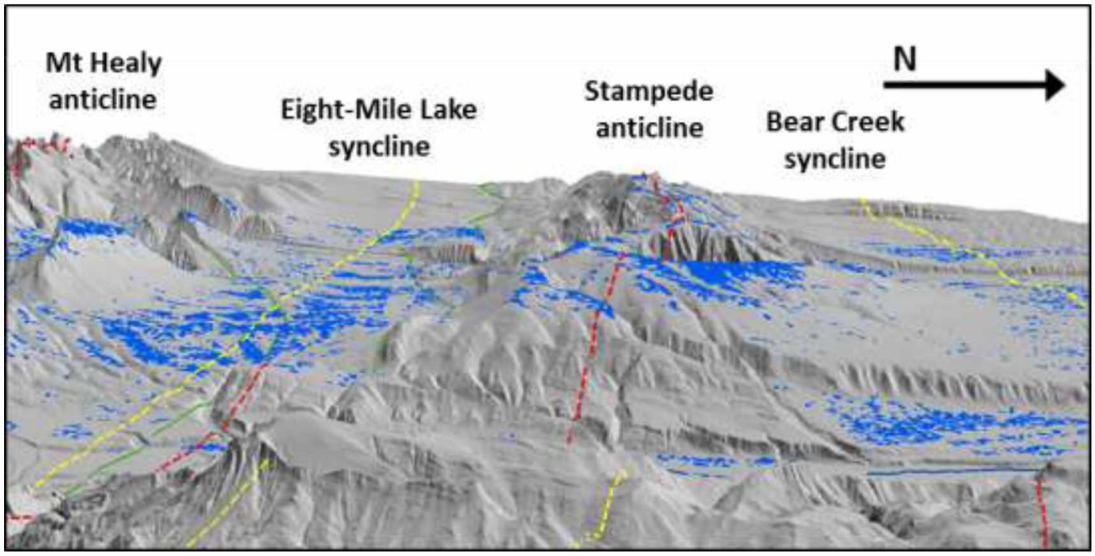

Figure 6.4 Extracted Surface Overlay, Nenana River Area. The overlay in the Nenana River region of the study area shows clear deformation of the preserved surface (blue) along the synclines (yellow hashed lines) and anticlines (red hashed lines) in the area.

6.2 Longitudinal River Profiles

To create the longitudinal river profiles, I digitized 135 streams and rivers in the study area from the USGS 1:63,360-scale topographic maps. I then overlaid the drainage traces on top of the InSAR DEM mosaic and extracted elevation data along the river trace. I chose the longitudinal profiles for St. George Creek, Gold King Creek, Fish Creek

and a tributary to Fish Creek (Figure 6.5) for analysis, because all of these streams cross known structures and show significant deviation from the ideal profile in the vicinity of the faults and anticlines.

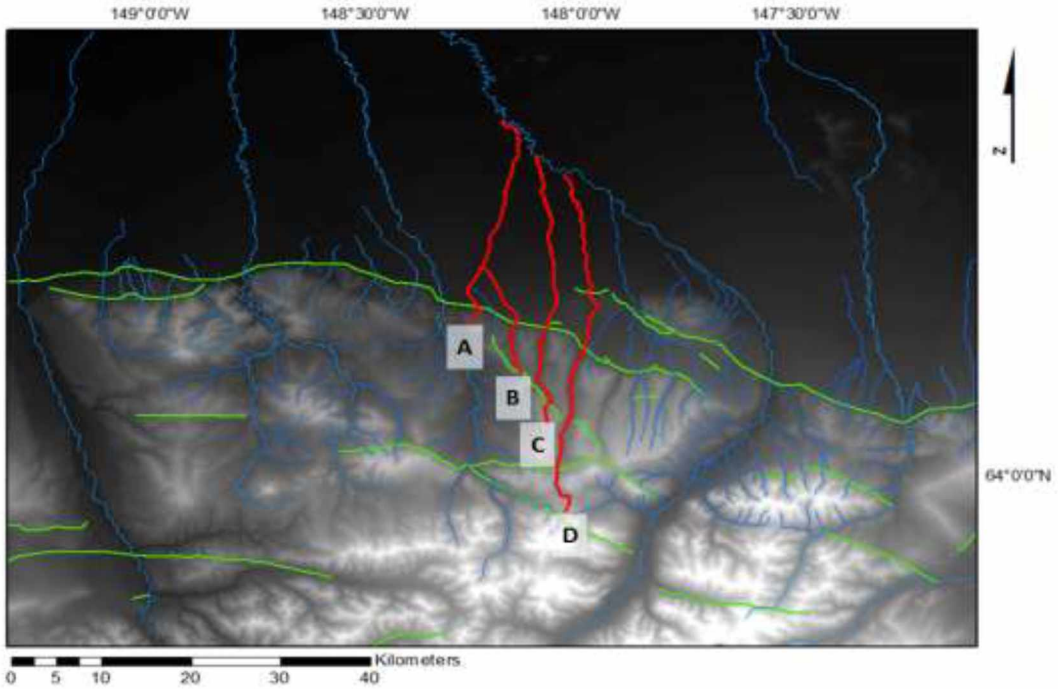

Figure 6.5 Locations of Longitudinal River Profiles. Study area DEM with faults (green) and rivers (blue). The streams used for visual analysis of longitudinal profiles are highlighted in red. A) Fish Creek, B) Tributary to Fish Creek, C) Gold King Creek and D) St. George Creek.

Each stream shows deflection from an ideal river profile (black lines in Figure 6.5), which indicates ongoing deformation in the area. The ideal profile was mathematically generated and fit to the stream in Excel. The streams show a distinct convexity along the middle reach of the profile (Figure 6.5), except for Fish Creek (Stream A). Fish Creek's drainage starts closer to the northern edge of the foothills, so it displays a shorter convexity in addition to a significant deflection from the ideal profile where it crosses

the Northern Foothills thrust. This convexity also seems to be related to the presence of the Rex and Japan Hills anticlines as there is a drop-off on the profiles following the trace of the Japan Hills splay. The Fish Creek and the Fish Creek tributary cross what could be an inferred Japan Hills splay to the west of St. George Creek, where the profiles seem to steepen.

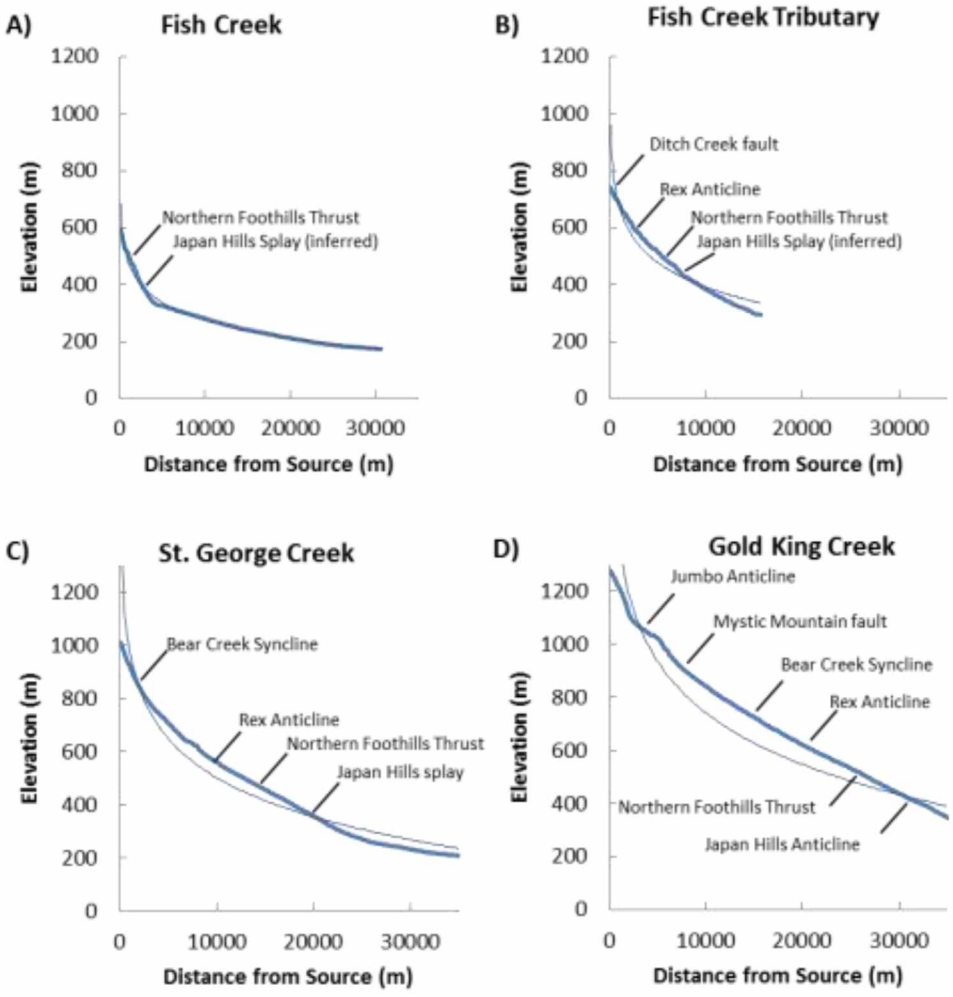

Figure 6.6 Longitudinal River Profiles. Longitudinal profiles of Fish Creek (A), Fish Creek tributary (B), St. George Creek (C), and Gold King Creek (D), with locations of structures. Each profile shows a convexity south of the Northern Foothills thrust fault that is largely a reflection of the Rex anticline.

6.3 Stream Length-Gradient Index

Because there was a visible deflection in the longitudinal profiles I calculated the SL index for the 135 streams and rivers for which I created longitudinal profiles (see Appendix A for procedure for calculating the SL index). Due to the high concentration of small streams and tributaries in the study area and the inherent error in the SL index in the lower reaches of higher order rivers (Perez-Pena et al., 2010), I omitted the larger rivers in the study area, such as the Nenana, Totatlanika and Wood Rivers (Figure 6.7, red rivers). I then overlaid the remaining streams (Figure 6.7, blue rivers) on the 10 meter DEM and sampled elevations at 7 meter horizontal intervals along the profile. I then averaged the data along the streams to create a data point at 70 meter intervals and calculated the SL Index from the elevations at those points relative to the stream source. The SL index was then plotted along the stream and interpolated across the foothills using ArcMap. Rivers, streams, folds and faults were then overlain on the SL index map to assess correlations with known faults in the region.

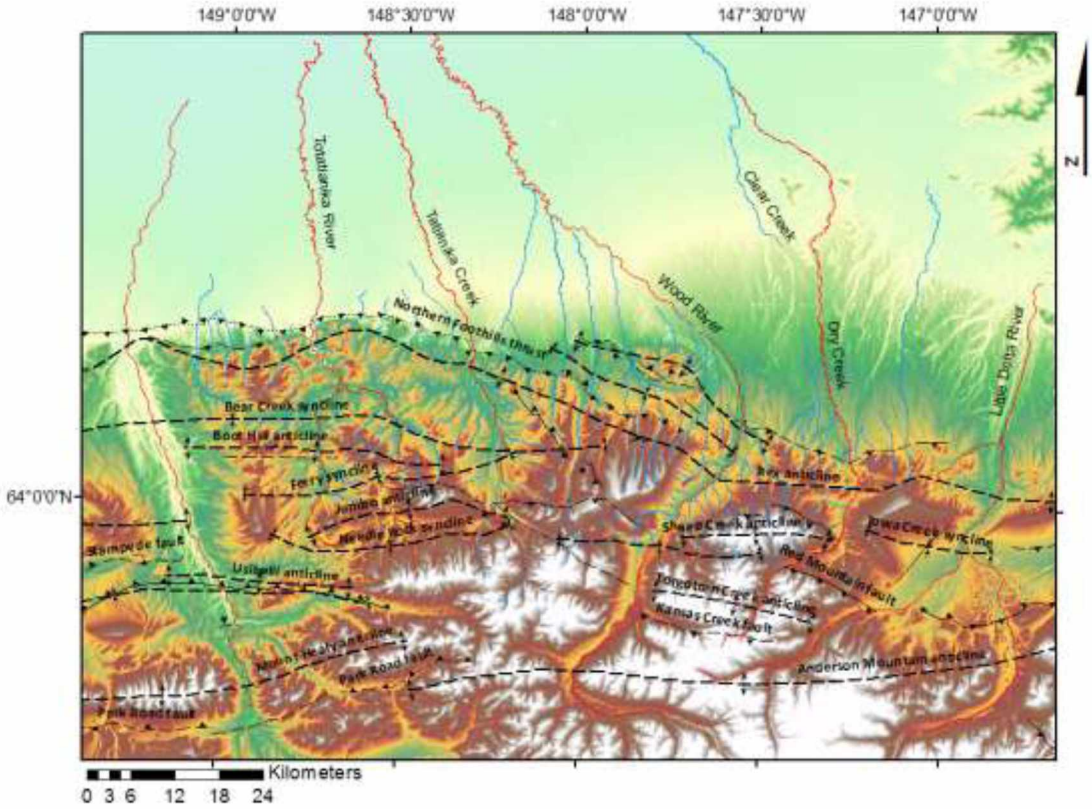

Figure 6.7 Rivers, Folds and Faults in the SL Index Study Area. Map shows the locations of the digitized rivers for the SL index map. Higher order rivers and creeks shown here in red have been omitted from the SL index map while smaller waterways that were used are in blue. Faults and folds are labeled.

Anomalies in the SL Index are colored green and yellow on the map and tend to correlate with faults and anticlines in the area (Figure 6.8). One noticeable trend is defined by spots with higher SL Index values along the Rex anticline from east to west, indicating this to be an actively growing structure. Another notable area of high index values is in the area of the western part of the Gold King fault, to the west of the Japan Hills. Two parts of the Gold King fault intersect here in an area known to be structurally complex (Bemis et al., 2012). The SL indices seem to confirm activity in the area,

perhaps reflecting growth of the Japan Hills anticline. To the south of the Japan Hills, high indices coincide with the uplifted side of the Bear Creek fault and to the southwest of that, high indices coincide with the confluence of the Jumbo anticline, Needle Rock syncline, Mystic Mountain syncline and the Kansas Creek fault. Other notable areas where high SL Indices are associated with structure are near the Glacier Creek and Red Mountain faults. With the coincidence of SL Index values and known structure, the SL Index map appears to be a good way to locate areas of increased tectonic activity.

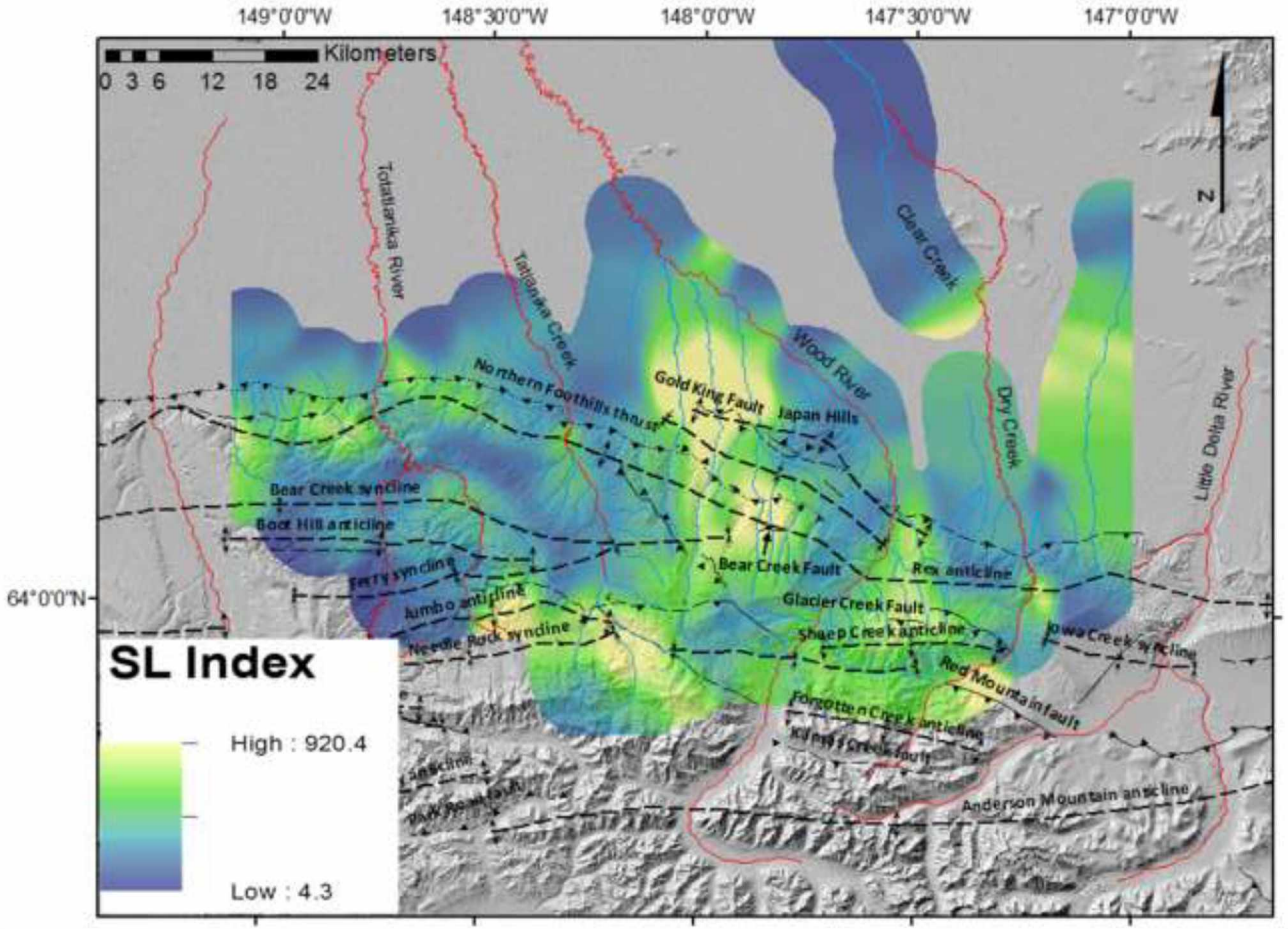

Figure 6.8 SL Index Map. Overlay of interpolated stream length indices on a hillshade image, showing areas with high SL Index values. Indicating stream deviation from a normal profile in yellow. Excluded rivers are in red, while measured rivers are in blue. Faults and folds are shown in black and identified with appropriate structural symbols.

6.4 Combined Analysis

Finally, I combined the data from the polarimetric SAR classification with the SL Indices map. When these data are combined, the warmer colors of the SL Index coincide with the extracted classified preserved surface. Because the SL Index is based on the structural changes and uplift in the area and the preserved surface is a result of that activity over time, the two elements should inherently be correlated. This can be seen in figure 6.9 in the areas of the Needle Rock syncline, Kansas Creek fault, Red Mountain fault, Glacier Creek fault, and along the Rex anticline. Although there is a correlation between the two elements, there are also areas where the SL Index is high but the SAR data do not indicate the presence of preserved Nenana Gravel. This can be attributed to the fact that there is tectonic activity in areas where the gravel may have been previously eroded, recently covered, or was never deposited, such as in the Sheep Creek anticline and near the headwaters of Dry Creek. Where the Nenana Gravel has been preserved and the SL Index is high are key areas where future research and fieldwork may be concentrated to study local tectonics and neotectonic mechanisms.

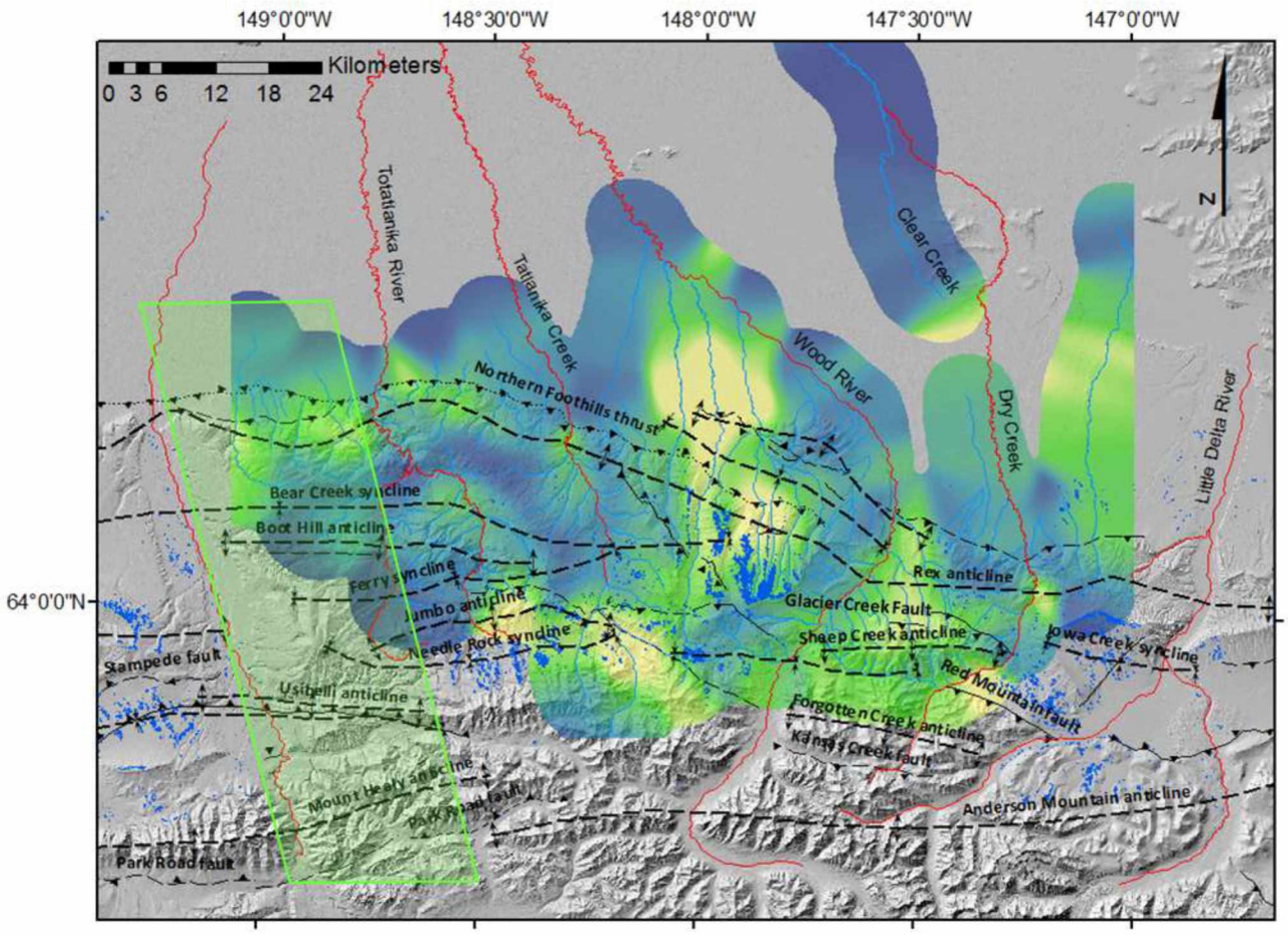

Figure 6.9 Combination of SL Index Map and Preserved Surface. Overlay of SL Index map and extracted preserved surface onto the hillshade image. It can be seen that the high SL values and the preserved surface coincide in several places. The green box indicates area of missing SAR.

7.0 Conclusions

This study resulted in several positive conclusions: (1) that polarimetric SAR can be successfully mosaicked and (2) that this data can be used for geologic classification. Although I had to exclude a portion of the study area because of weather and a lack of data, (3) an extensive area of the preserved Nenana Gravel could be correctly classified and overlain on the current DEM's of the area. (4) When this data was overlain on the DEM, the extracted preserved Nenana Gravel areas correlated well with known tectonic features in the region. This provides additional evidence of the quality of the classification procedure and also lets me conclude that the extracted Nenana Gravel surfaces can be used to discern the geometry of the young structural deformation in the area. (5) Use of the newly released DEM's allowed a high resolution Stream Length-Gradient Index map to be created without the need for extensive fieldwork, although testing sites in the field to determine accuracy would be a good addition to the procedure. With the success of the polarimetric SAR classification and the association of anomalous SL indices with nearby faults and folds, I conclude that it is feasible to use the newly released DEM and available SAR data to indicating the location of neotectonic activity. These processes can be utilized on a regional scale to determine where future studies should be concentrated.

8.0 References

Alaska Satellite Facility. "SAR Data Center (SDC)." *Welcome to Alaska Satellite Facility*, 2013. Web. 22 Feb. 2013.

Athey, J.E., Newberry, R.J., Werdon, M.B., Freeman, L.K., Smith, R.L., and Szumigala, D.J. *Bedrock geologic map of the Liberty Bell area, Fairbanks A-4 Quadrangle, Bonnifield mining district, Alaska.* Map. Fairbanks, AK: Alaska Division of Geological & Geophysical Surveys, 2006. Print. 1:50,000.

Atwood, D. K., D. Small, and R. Gens. "Improving PolSAR Land Cover Classification With Radiometric Correction of the Coherency Matrix." *IEEE Journal of Selected Topics in Applied Earth Science Observations and Remote Sensing* 5.3 (2012): 848-56. Print.

Azor, A., E. A. Keller, and R. S. Yeats. "Geomorphic Indicators of Active Fold Growth: South Mountain–Oak Ridge Anticline, Ventura Basin, Southern California." *Geological Society of America Bulletin* 114.6 (2002): 745-53. Print.

Bayer, T., R. Winter, and G. Schreier. "Terrain Influences in SAR Backscatterand Attempts to Their Correction." *IEEE Transactions on Geoscience and Remote Sensing* 29.3 (1991): 451-62. Print.

Bemis, S. P. *Neotectonic Framework of the North-central Alaska Range Foothills*. Thesis. University of Alaska Fairbanks, 2004. Print.

Bemis, S. P. *Moletrack Scarps to Mountains: Quaternary Tectonics of the Central Alaska Range*. Diss. University of Oregon, 2010. Print.

Bemis, S. P., and W. K. Wallace. "Neotectonic Framework of the North-central Alaska Range Foothills." Ed. K. Ridgway, J. Trop, J. Glen, and M. Fisher. *Tectonic Growth of a Collisional Continental Margin: Crustal Evolution of Southern Alaska, Geological Society of America Special Paper 431* (2007): 549-72. Print.

Bemis, S. P., G. A. Carver, and R. D. Koehler. "The Quaternary Thrust System of the Northern Alaska Range." *Geosphere* 8.1 (2012): 1-10. Print.

Big Delta (A-6) Quadrangle, Alaska. Map. Reston, VA: U.S. Dept. of the Interior, U.S. Geological Survey, 1949. Print. 1:63,360 Series (Topographic).

Big Delta (B-6) Quadrangle, Alaska. Map. Reston, VA: U.S. Dept. of the Interior, U.S. Geological Survey, 1949. Print. 1:63,360 Series (Topographic).

Castleman, K. R. *Digital Image Processing*. Englewood Cliffs, NJ: Prentice-Hall, 1996. Print.

Cui, Y., Y. Yamaguchi, J. Yang, S. Park, H. Kobayashi, and G. Singh. "Three-Component Power Decomposition for Polarimetric SAR Data Based on Adaptive Volume Scatter Modeling." *Remote Sensing* 4 (2010): 1559-572. Print.

Duchossois, G., and P. Martin. "ERS-1 and ERS-2 Tandem Operations." *ERS-1 and ERS-2 Tandem Operations*. European Space Agency. Web. 18 Jan. 2012.

Dusel-Bacon, C., J. L. Wooden, and M. J. Hopkins. "U-Pb Zircon and Geochemical Evidence for Bimodal Mid-Paleozoic Magmatism and Syngenetic Base-metal Mineralization in the Yukon-Tanana Terrane, Alaska." *Geological Society of America Bulletin* 116.7 (2004): 989. Print.

Fairbanks (A-1) Quadrangle, Alaska. Map. Reston, VA: U.S. Dept. of the Interior, U.S. Geological Survey, 1949. Print. 1:63,360 Series (Topographic).

Fairbanks (A-2) Quadrangle, Alaska. Map. Reston, VA: U.S. Dept. of the Interior, U.S. Geological Survey, 1950. Print. 1:63,360 Series (Topographic).

Fairbanks (A-3) Quadrangle, Alaska. Map. Reston, VA: U.S. Dept. of the Interior, U.S. Geological Survey, 1950. Print. 1:63,360 Series (Topographic).

Fairbanks (A-4) Quadrangle, Alaska. Map. Reston, VA: U.S. Dept. of the Interior, U.S. Geological Survey, 1950. Print. 1:63,360 Series (Topographic).

Fairbanks (A-5) Quadrangle, Alaska. Map. Reston, VA: U.S. Dept. of the Interior, U.S. Geological Survey, 1950. Print. 1:63,360 Series (Topographic).

Fairbanks (B-1) Quadrangle, Alaska. Map. Reston, VA: U.S. Dept. of the Interior, U.S. Geological Survey, 1950. Print. 1:63,360 Series (Topographic).

Fairbanks (B-2) Quadrangle, Alaska. Map. Reston, VA: U.S. Dept. of the Interior, U.S. Geological Survey, 1950. Print. 1:63,360 Series (Topographic).

Fairbanks (B-3) Quadrangle, Alaska. Map. Reston, VA: U.S. Dept. of the Interior, U.S. Geological Survey, 1949. Print. 1:63,360 Series (Topographic).

Fairbanks (B-4) Quadrangle, Alaska. Map. Reston, VA: U.S. Dept. of the Interior, U.S. Geological Survey, 1949. Print. 1:63,360 Series (Topographic).

Fairbanks (B-5) Quadrangle, Alaska. Map. Reston, VA: U.S. Dept. of the Interior, U.S. Geological Survey, 1950. Print. 1:63,360 Series (Topographic).

Fairbanks (C-2) Quadrangle, Alaska. Map. Reston, VA: U.S. Dept. of the Interior, U.S. Geological Survey, 1949. Print. 1:63,360 Series (Topographic).

Fairbanks (C-3) Quadrangle, Alaska. Map. Reston, VA: U.S. Dept. of the Interior, U.S. Geological Survey, 1949. Print. 1:63,360 Series (Topographic).

Fairbanks (C-4) Quadrangle, Alaska. Map. Reston, VA: U.S. Dept. of the Interior, U.S. Geological Survey, 1950. Print. 1:63,360 Series (Topographic).

Farr, T. G., P. A. Rosen, E. Caro, R. Crippen, R. Duren, S. Hensley, M. Kobrick, M. Paller, E. Rodriguez, L. Roth, D. Seal, S. Shaffer, J. Shimada, J. Umland, M. Werner, M. Oskin, D. Burbank, and D. Alsdorf. "The Shuttle Radar Topography Mission." *Reviews of Geophysics* 45.2 (2007): 43. Print.

Font, M., D. Amorese, and J. Lagarde. "DEM and GIS Analysis of the Stream Gradient Index to Evaluate Effects of Tectonics: The Normandy Intraplate Area (NW France)." *Geomorphology* 119.3-4 (2010): 172-80. Print.

Freymueller, J. T., H. Woodard, S. C. Cohen, R. Cross, J. Elliot, C. F. Larson, S. Hreinsdottir, and C. Zweck. "Active Deformation Processes in Alaska, Based on 15 Years of GPS Measurements." Ed. J. T. Freymueller and Al. Et. *Active Tectonics and Seismic Potential of Alaska: American Geophysical Union Geophysical Monograph* 179 (2008): 1-42. Print.

Gens, R. "SAR: Principles and Applications." 2008. Lecture.

Gens, R., D. K. Atwood, and E. Pottier. "Geocoding of Polarimetric Processing Results: Alternative Processing Strategies." *Remote Sensing Letters* 4.1 (2013): 39-45. Print.

Gesch, D., Evans, G., Mauck, J., Hutchinson, J., Carswell Jr., W.J., 2009, *The National Map*—Elevation: U.S. Geological Survey Fact Sheet 2009-3053, 4 p. Web. 2012

Hack, T. J. "Stream-profile Analysis and Stream-gradient Index." *U.S. Geological Survey Journal Research* 1.4 (1973): 421-29. Print.

Haeussler, P. J. "An Overview of the Neotectonics of Interior Alaska—Far-field Deformation from the Yakutat Microplate Collision." Ed. J. T. Freymueller, P. J. Haeussler, R. L. Wesson, and G. Ekstrom. *Active Tectonics and Seismic Potential of Alaska: American Geophysical Union, Geophysical Monograph* 179 (2008): 83-108. Print.

Hanson, K.L., Wells, D.L., Angell, M., 2002, "Activity of the Northern Foothills Thrust Fault: Strain Partitioning Related to the Denali Fault, Central Alaska." American Geophysical Union, Fall Meeting 2002, abstract #S72F-1333

Hanssen, R. F. *Radar Interferometry: Data Interpretation and Error Analysis*. Dordrecht: Kluwer Academic, 2001. Print.

Healy (D-1) Quadrangle, Alaska. Map. Reston, VA: U.S. Dept. of the Interior, U.S. Geological Survey, 1949. Print. 1:63,360 Series (Topographic).

Healy (D-2) Quadrangle, Alaska. Map. Reston, VA: U.S. Dept. of the Interior, U.S. Geological Survey, 1951. Print. 1:63,360 Series (Topographic).

Healy (D-3) Quadrangle, Alaska. Map. Reston, VA: U.S. Dept. of the Interior, U.S. Geological Survey, 1950. Print. 1:63,360 Series (Topographic).

Healy (D-4) Quadrangle, Alaska. Map. Reston, VA: U.S. Dept. of the Interior, U.S. Geological Survey, 1950. Print. 1:63,360 Series (Topographic).

Healy (D-5) Quadrangle, Alaska. Map. Reston, VA: U.S. Dept. of the Interior, U.S. Geological Survey, 1951. Print. 1:63,360 Series (Topographic).

Healy (D-6) Quadrangle, Alaska. Map. Reston, VA: U.S. Dept. of the Interior, U.S. Geological Survey, 1954. Print. 1:63,360 Series (Topographic).

Japan Aerospace Exploration Agency. "About ALOS." *About ALOS*. Japan Aerospace Exploration Agency, 1997. Web. 22 Feb. 2013.

Keller, E. A., and N. Pinter. *Active Tectonics: Earthquakes, Uplift, and Landscapes*. 2nd ed. Englewood Cliffs, NJ: Prentice-Hall, 2002. Print.

Keller, E. A., D. B. Seaver, D. L. Laduzinsky, D. L. Johnson, and T. L. Ku. "Tectonic Geomorphology of Active Folding over Buried Reverse Faults: San Emigdio Mountain Front, Southern San Joaquin Valley, California." *Geological Society of America Bulletin* 112.1 (2000): 86-97. Print.

Larue, J. "Longitudinal Profiles and Knickzones: The Example of the Rivers of the Cher Basin in the Northern French Massif Central." *Proceedings of the Geologists' Association* (2010). Print.

Lee, J., and E. Pottier. *Polarimetric Radar Imaging: From Basics to Applications*. Boca Raton: CRC, 2009. Print.

Lesh, M. E. *Neotectonics and stratigraphy of the Alaska Range foreland basin and cross-section of southern Alaska.* Thesis. Prudue University, 2002. Print.

Lesh, M. E., and K. D. Ridgway. "Geomorphic Evidence of Active Transpressional Deformations in the Tanana Foreland Basin, South-central Alaska." *The Geologic Society of America, Special Paper* 431 (2007): 573-92. Print.

Lillesand, Thomas M., Ralph W. Kiefer, and Jonathan W. Chipman. Remote Sensing and Image Interpretation. Hoboken, NJ: John Wiley & Sons, 2008. Print.

McAlpin, D., and F. J. Meyer. "Multi-sensor Data Fusion for Remote Sensing of Post-eruptive Deformation and Depositional Features at Redoubt Volcano." *Journal of Volcanology and Geothermal Research* (2012): 10. Web. 2012

Merritts, D., and K. R. Vincent. "“Geomorphic Response of Coastal Streams to Low, Intermediate, and High Rates of Uplift, Mendocino Triple Junction Region, Northern California." *Geological Society of America Bulletin* 101 (1989): 1373-388. Print.

Meyer, F, J., "Principles and Applications of Radar Remote Sensing." 2009. Lecture.

Meyer, F. J., and D. T. Sandwell. "SAR Interferometry at Venus for Topography and Change Detection." *Planetary and Space Science* 73.1 (2012): 130-44. Print.

Mt. Hayes (C-6) Quadrangle, Alaska. Map. Reston, VA: U.S. Dept. of the Interior, U.S. Geological Survey, 1951. Print. 1:63,360 Series (Topographic).

Mt. Hayes (D-6) Quadrangle, Alaska. Map. Reston, VA: U.S. Dept. of the Interior, U.S. Geological Survey, 1950. Print. 1:63,360 Series (Topographic).

Pérez-Peña, J. Vicente, A. Azor, J. M. Azañón, and E. A. Keller. "Active Tectonics in the Sierra Nevada (Betic Cordillera, SE Spain): Insights from Geomorphic Indexes and Drainage Pattern Analysis." *Geomorphology* 119.1-2 (2010): 74-87. Print.

Ridgway, K. D., E. E. Thoms, P. W. Layer, M. E. Lesh, J. M. White, and S. V. Smith. "Neogene Transpressional Foreland Basin Development on the North Side of the Central Alaska Range, Usibelli Group and Nenana Gravel, Tanana Basin." Ed. K. Ridgway, J. Trop, J. Glen, and M. Fisher. *Tectonic Growth of a Collisional Continental Margin: Crustal Evolution of Southern Alaska, Geological Society of America Special Paper 431* (2007): 507-48. Print.

Seeber, L., and V. Gornitz. "River Profiles along the Himalayan Arc as Indicators of Active Tectonics." *Tectonophysics* 92.4 (1983): 335-67. Print.

Small, D. "Flattening Gamma: Radiometric Terrain Correction for SAR Imagery." *IEEE Transactions on Geoscience and Remote Sensing* 49.8 (2011): 3081-093. Print.

Takaku, J., and T. Tadono. "PRISM On-Orbit Geometric Calibration and DSM Performance." *IEEE Transactions on Geoscience and Remote Sensing* 47.12 (2009): 4060-073. Print.

Triplehorn, D. M., J. Drake, and P. W. Layer. "Preliminary 40Ag/39Ag Ages from Two Units in the Usibelli Group, Healy, Alaska: New Light on Some Old Problems." *Short Notes on Alaska Geology* 1999 (2000): 117-27. Print.

Wahrhaftig, C. “Quaternary geology of the Nenana River and adjacent parts of the Alaska Range, Alaska”: *U.S. Geological Survey Open-File Report* 53-262 (1953): 163. Print.

Wahrhaftig, C. “Schists of the central Alaska Range.” *U.S. Geological Survey Bulletin* 1254-E (1968): E1-E22. Print

Wahrhaftig, C. *Geologic map of the Fairbanks A-2 quadrangle, Alaska.* Map. Reston, VA: U.S. Dept. of the Interior, U.S. Geological Survey, 1970a. Print. 1:63,360.

Wahrhaftig, C. *Geologic map of the Fairbanks A-3 quadrangle, Alaska.* Map. Reston, VA: U.S. Dept. of the Interior, U.S. Geological Survey, 1970b. Print. 1:63,360.

Wahrhaftig, C. *Geologic map of the Fairbanks A-4 quadrangle, Alaska.* Map. Reston, VA: U.S. Dept. of the Interior, U.S. Geological Survey, 1970c. Print. 1:63,360.

Wahrhaftig, C. *Geologic map of the Fairbanks A-5 quadrangle, Alaska.* Map. Reston, VA: U.S. Dept. of the Interior, U.S. Geological Survey, 1970d. Print. 1:63,360.

Wahrhaftig, C. *Geologic map of the Healy D-2 quadrangle, Alaska.* Map. Reston, VA: U.S. Dept. of the Interior, U.S. Geological Survey, 1970e. Print. 1:63,360.

Wahrhaftig, C. *Geologic map of the Healy D-3 quadrangle, Alaska.* Map. Reston, VA: U.S. Dept. of the Interior, U.S. Geological Survey, 1970f. Print. 1:63,360.

Wahrhaftig, C. *Geologic map of the Healy D-4 quadrangle, Alaska.* Map. Reston, VA: U.S. Dept. of the Interior, U.S. Geological Survey, 1970g. Print. 1:63,360.

Wahrhaftig, C. *Geologic map of the Healy D-5 quadrangle, Alaska.* Map. Reston, VA: U.S. Dept. of the Interior, U.S. Geological Survey, 1970h. Print. 1:63,360.

Wahrhaftig, C. "The Cenozoic section at Suntrana, Alaska." Ed. M.L. Hill, *Geological Society of America, Cordilleran Section, Central Field Guide*, 1 (1987): 445-450. Print.

Wilson, F. H., J. H. Dover, D.C. Bradley, F. R. Weber, T. K. Bundtzen, and P. J. Haeussler Geologic Map of Centeral (Interior) Alaska. Map. Reston, VA: U.S. Dept. of the Interior, U.S. Geological Survey, 1998. Print. 1:500,000.

Woodhouse, I. H. *Introduction to Microwave Remote Sensing*. Boca Raton: Taylor & Francis, 2006. Print.

Yamaguchi, Y., T. Moriyama, M. Ishido, and H. Yamada. "Four-component Scattering Model for Polarimetric SAR Image Decomposition." *IEEE Transactions on Geoscience and Remote Sensing* 43.8 (2005): 1699-706. Print.

Yamaguchi, Y., Y. Yajima, and H. Yamada. "A Four-Component Decomposition of POLSAR Images Based on the Coherency Matrix." *IEEE Geoscience and Remote Sensing Letters* 3.3 (2006): 292-96. Print.

APPENDIX

Procedure for collecting longitudinal river profiles for SL Index Mapping

1. Digitize streams and rivers into poly lines in ArcMap, from the georeferenced USGS topographic maps.
2. Import river vectors and mosaicked DEM into PCI Geomatica.
3. Select individual river vector for profile on DEM.
4. Export profile to text file. Text data has distance from the vector start point (head of stream), elevation and UTM latitude and longitude for that point.
5. Import text file into Excel spreadsheet.
6. Average values to 10x's the original sampling.
7. Apply Hack's SL Index equation to averaged points.
8. Import compiled SL Index data from Excel including Easting, Northing, and SL Index value, as "XY data"
9. Export this data to a shape file and add to map
10. Using the Geostatistical Tools choose Diffusion Interpolation with Barrier keeping default parameters.
11. Run.